universität wien

MASTERARBEIT / MASTER'S THESIS

Titel der Masterarbeit / Title of the Master's Thesis

Upgrade of the experimental apparatus "VIP2" to test the Violation of the Pauli Exclusion Principle

verfasst von / submitted by

Alen Lika, BSc

angestrebter akademischer Grand / in partial fulfilment of the requirements for the degree of

Master of Science (MSc)

Wien, 2019 / Vienna, 2019

Studienkennzahl lt. Studienblatt / degree programme code as it appears on the student record sheet:	A 066 876
Studienrichtung lt. Studienblatt / degree programme as it appears on the student record sheet:	Masterstudium Physik
Betreut von / Supervisor:	Priv.-Doz. Dr. Johann Zmeskal
Mitbetreut von / Co-Supervisor:	

Abstract

The Pauli Exclusion Principle (PEP) is a fundamental principle in physics, governing the behavior of fermionic particles. Due to its importance, it needs to be tested as precisely as possible. In a pioneering experiment, Ramberg and Snow supplied an electric current to a Cu target and searched for PEP violating atomic transitions of "fresh" electrons from the current. As these transitions are only expected when the current is on, the difference between the spectra with and without current can be used to set an upper limit for the probability for the violation of the PEP. Specifically, the experiment searched for forbidden K_α transitions, which have a slightly lower transition energy than the normal transitions. Photons from these transitions can therefore be distinguished by their energy. The VIP2 (Violation of the Pauli Exclusion Principle) experiment could set this upper limit to 1.87×10^{-29} with the described method. The VIP2-Upgrade experiment wants to improve this limit by upgrading crucial components of the setup.

The upgrade focused on improving the overall cooling system, slow control system and active shielding. The original idea for upgrading the cooling system involved a three step peltier cooling device to cool the new Silicon Drift Detectors (SDDs) to a temperature of at least $-40°C$ or lower, which proved not to be able to deliver the required cooling capacity needed for the SDDs. Instead we decided to use the Polycold Compact Cooler (CryoTiger), manufactured by Brooks Automation, which gave us more than enough ($-80°C$) cooling capacity (even with the heat load of the SDDs) for our required purposes. A Slow Control system using LabVIEW was built for monitoring the vacuum pressure as well as all temperature sensors (PT-100) installed within the VIP2-Upgrade experimental setup. Additionally, the active shielding, which was used for three years during the predecessor experiment VIP2, was tested and the results showed that almost a third of the Silicon Photomultipliers (SiPMs) used were ineffective and needed to be either repaired or replaced. Therefore, we decided to use passive shielding instead, while the active shielding will be repaired or upgraded.

After exhaustive testing with the VIP2-Upgrade experimental setup, which included a lot of vacuum testing, it was transported to the underground laboratory of Gran Sasso (LNGS). The setup was successfully installed and the first measurements were started. The setup is currently collecting data, which we can access using a remote control system connection from the Stefan Meyer Institute (SMI) to the VIP2 laboratory at LNGS.

Zusammenfassung

Das Pauli-Prinzip (Pauli-Verbot) ist ein Grundprinzip in der Physik, welches das Verhalten fermionischer Teilchen regelt. Aufgrund seiner Bedeutung muss es so genau wie möglich getestet werden. In einem bahnbrechenden Experiment versorgten Ramberg und Snow ein Cu-Target mit einem elektrischen Strom und suchten nach Pauli-Verbot-verletzenden Atomübergängen "frischer" Elektronen aus dem Strom durch das Cu-Target. Da diese Übergänge nur bei eingeschaltetem Strom zu erwarten sind, kann mit der Differenz zwischen den Spektren mit und ohne Strom eine Obergrenze für die Wahrscheinlichkeit der Verletzung des Pauli-Verbots gesetzt werden. Insbesondere suchte man nach Verbotenen K_α Übergängen, die eine etwas niedrigere Übergangsenergie als die normalen Übergänge haben. Photonen aus diesen Übergängen können daher durch ihre Energie unterschieden werden. Das VIP2 Experiment (Verletzung des Pauli-Verbots) könnte diese Obergrenze mit der beschriebenen Methode auf 1.87×10^{-29} setzen. Das VIP2-Upgrade-Experiment will dieses Limit durch ein Upgrade wichtiger Komponenten des Setups noch weiter verbessern.

Das Upgrade konzentrierte sich auf die Verbesserung des Kühlsystems, des Slow Control Systems sowie der aktiven Abschirmung. Die ursprüngliche Idee zur Verbesserung des Kühlsystems bestand in einem dreistufigen Peltier-Kühlgerät, um die neuen Silizium-Drift-Detektoren (SDDs) auf eine Temperatur von mindestens $-40°C$ oder weniger zu kühlen. Nach ersten Tests entschieden wir uns für den PolyCold Compact Cooler (CryoTiger) von Brooks Automation, der mehr als genug ($-80°C$) Kühlleistung (auch bei der Wärmelast der SDDs) erreichte. Ein Slow Control System wurde mit LabVIEW entwickelt um alle Temperatursensoren (PT-100) und den Vakuumdruck im VIP2-Upgrade-Versuchsaufbau zu überwachen. Zusätzlich wurde das aktive Abschirmsystem, das im Vorgänger-Experiment VIP2 drei Jahre lang eingesetzt wurde, getestet und die Ergebnisse zeigten, dass fast ein Drittel der eingesetzten Silizium-Photomultiplier (SiPMs) defekt waren und entweder repariert oder ersetzt werden müssen. Daher haben wir beschlossen, stattdessen ein passives Abschirmsystem zu verwenden, während die aktive Abschirmung repariert oder aufgerüstet wird.

Nach ausführlichen Tests mit dem VIP-Upgrade-Versuchsaufbau, der viele Vakuumtests beinhaltete, wurde es in das unterirdische Labor von Gran Sasso (LNGS) transportiert. Das Setup wurde erfolgreich installiert und die ersten Messungen wurden gestartet. Die Apparatur sammelt derzeit Daten, auf die wir über eine Netzwerkverbindung vom Stefan Meyer Institut (SMI) zum VIP2-Labor bei LNGS zugreifen können.

Acknowledgements

First of all I want to thank my supervisor Dr. Johann Zmeskal who spent a lot of time answering my questions, thinking about my problems and constantly encouraging and guiding me throughout my master's.

I also want to thank Prof. Eberhard Widmann, who has provided this opportunity for me. Furthermore, I would like to thank Andreas, Michael, Doris, Leo and Mark for their help during this time, along with all the other colleagues of SMI, including all of the students that were involved with this work.

Without my friends Deniz, Amil, Armin, Lukas and Ivan my university career would not have been the same. Thank you for all the long conversations, support and always pushing me to be the best version of myself.

Last but not least, I wish to thank my family, without whom all of this would not have been possible. I will never be able to express my gratitude with words and I would not be who I am without them. I want to specifically mention my sister Izabela, who has the gift of always making me smile when nobody else can.

Contents

Chapter 1

Introduction and Motivation

The Pauli Exclusion Principle (PEP) is a fundamental principle in physics, valid for identical-fermion systems. It was formulated in 1925 by the Austrian physicist Wolfgang Pauli. It states that two fermions (particles with half integer spin) can not occupy the same quantum state simultaneously. Examples of fermionic particles are elementary particles such as quarks, leptons (electron, muon and tauon) and neutrinos. Composite particles can also be fermions (e.g. protons and neutrons). Electrons, which make up the electronic shell of atoms, are fermions and therefore obey the PEP. For the case of electronic shells, the PEP is equivalent to the statement that two electrons cannot have the same principal quantum number, angular momentum quantum number l, magnetic quantum number m_l and spin quantum number m_s at the same time. This means that two electrons can share the quantum numbers n, l and m_l, as long as they have a different spin quantum number $m_s(\pm\frac{1}{2})$.

The PEP forms the basis of the periodic table of elements, as it prevents all electrons in a shell to condense into the ground state. Therefore, it is responsible for the occupation of the electronic shells and the chemical properties of elements. It also stabilizes neutron stars, as the neutron degeneracy pressure, which is caused by the PEP, prevents them from collapsing under their own gravitational pressure.

Due to the fundamental place of the PEP in quantum field theory, many researches were interested in testing it. In the year 1948, the PEP was tested by Goldhaber and Scharff-Goldhaber [1]. Their experiment was designed to determine if the particles making up β radiation were the same as electrons, but it was later interpreted as a test of the Pauli Exclusion Principle. The experiment was done by shining electrons from a β source onto a block of lead. The authors thought that if these β particles were different from electrons, they could be captured by the lead atoms and cascade down to the ground state without being subjected to the PEP. The fact that no X-rays were emitted during this process was used to set an upper bound for the probability that the PEP is violated. Another test was conducted in 1988 by E. Ramberg and G. A. Snow [2]. They introduced a current into a copper conductor. The electrons of the current then had a chance to be captured by the copper atoms and form a new quantum state. The experimenters searched for states having a symmetric component in an otherwise antisymmetric state. These states were identified by the X-rays they emitted during de-excitation to the ground state. Photons from these forbidden transitions were identified by their energy, which is

slightly shifted with respect to normal transitions. The same principle was later employed in the VIP experiment, which was able to set a new upper limit for the probability for the violation of the Pauli Exclusion Principle (parametrized in the literature by $\frac{\beta^2}{2}$) of

$$\frac{\beta^2}{2} \leq 4.17 \times 10^{-29}$$

([3],[4]).

The way I imagined this thesis to proceed is to start with a brief introduction and description of the VIP2 setup with all its elements including the cooling system, slow control system, active shielding and Silicon Drift Detectors (SDDs) in chapter 2. After that I would like to introduce the proposed upgrade, including all the testing and experimenting done at the Stefan Meyer Institute's (SMI) laboratory in chapter 3. Furthermore, the final setup of the VIP2-Upgrade experiment will be presented, in addition to some preliminary results in chapter 4. And lastly, chapter 5 will focus on a brief summary and a short outlook.

Chapter 2

Status of the Experimental Setup

Measuring energy spectra in the energy region where the PEP violating Kα transition is expected, is the main feature of the VIP2 setup. For such purposes Silicon Drift Detectors offer energy resolutions that are good enough to separate possible PEP violating Kα transitions from common ones, which (in copper) are 300 eV more energetic. Considering that SDDs offer a time resolution of $< 1\mu$s an active shielding was used, which consists of 32 plastic scintillator bars assembled around the copper target and the SDDs. Silicon Photomultipliers (SiPMs) were used to read out the light output coming from the scintillators. A cooling system, consisting of a helium compressor liquefying argon was keeping the required working temperature of the SDDs constant, which is around 150 K. Furthermore, a slow control system was monitoring crucial parameters of the experiment, while a data acquisition system was collecting data in the process. In Figure 2.1 a schematic drawing of the experiment can be seen. The most important components of the setup will be described in the following sections.

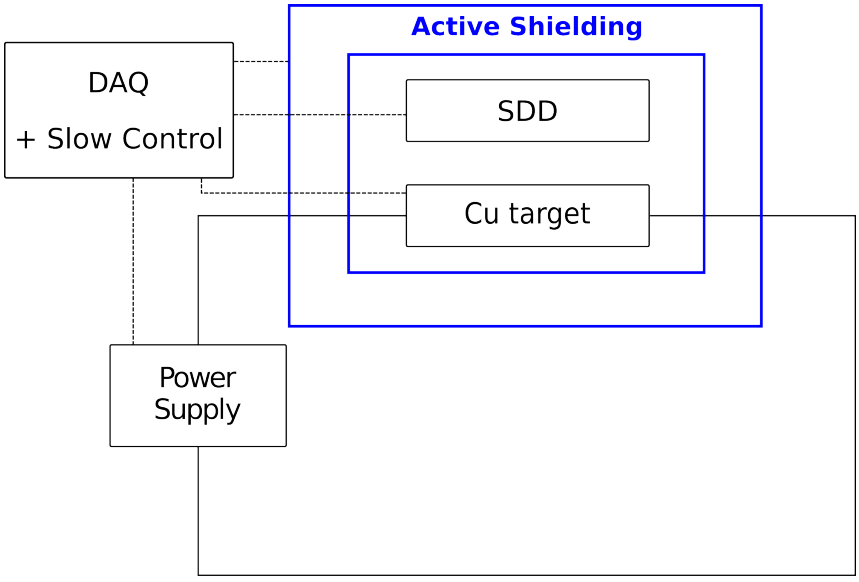

Figure 2.1: Schematic drawing of the VIP2 measurement setup [5].

2.1 Silicon Drift Detectors

Silicon Drift Detectors (SDDs) are used as X-ray detectors in the VIP2 setup. They are mounted as close as 5 mm away from the copper target to maximize solid angle coverage. The SDDs detect possible photons from PEP violating transitions in the Cu target introduced by the high current flowing through this target. The working principle of Silicon Drift Detectors is based on the sideward depletion, which was first introduced in [6]. In Figure 2.2 a schematic drawing of an SDD used for the VIP2 experiment is shown.

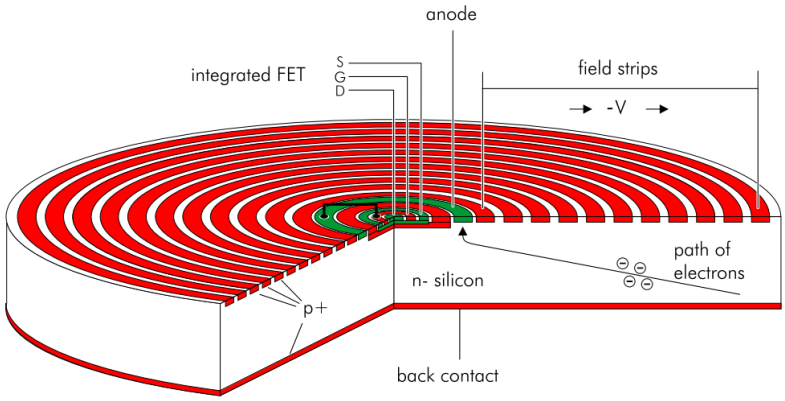

Figure 2.2: Schematic drawing of a Silicon Drift Detector [7].

On a cylindrical n-type silicon wafer, circular p^+-type silicon contacts are implanted on one flat surface. These contacts are used to apply an increasing reverse bias in order to fully deplete the wafer. The radiation entrance window is on the opposite side of the concentric contacts and consists of a homogeneous shallow junction, which gives homogeneous sensitivity over the whole surface. When photons or charged particles hit the silicon wafer, electron-hole pairs are generated. The free electrons fall to the lowest point of the potential produced by the concentric electrodes. This lowest point is the anode consisting of a ring close to the middle of the wafer. The amount of electrons generated in the wafer and collected by the anode is proportional to the energy of the radiation. By measuring the amount of charge collected this energy can be determined. The small size of the anode ensures a small anode capacitance, which is almost independent of the size of the detector [8] and only proportional to the anode's size. As some sources of noise are proportional to the capacitance [9] this reduces the noise and allows shorter shaping times, which in turn allows high count rates. As a first stage of amplification, a field effect transistor (FET) is integrated in the chip and connected to the anode by a metal strip. Thereby the capacitance between detector and amplifier is minimized and electric pickup noise is mostly avoided. The anode is discharged continuously. This avoids regular dead times of the detector by a repeating reset mechanism. The SDDs used in the VIP2 experiment consist of two arrays with three detector cells each. Each cell has an active area of 1 cm^2 shaped like a "rounded square" with a diameter of 10.3 mm and a corner radius of 2 mm. The maximum drift path length for electrons originating in a corner is 6.4 mm. The cells have a thickness of 450μm, which

ensures an absorption of 99% of 8 keV (Cu Kα line) X-rays. A schematic drawing of the front and back side of the arrays is shown in Figure 2.3 and Figure 2.4.

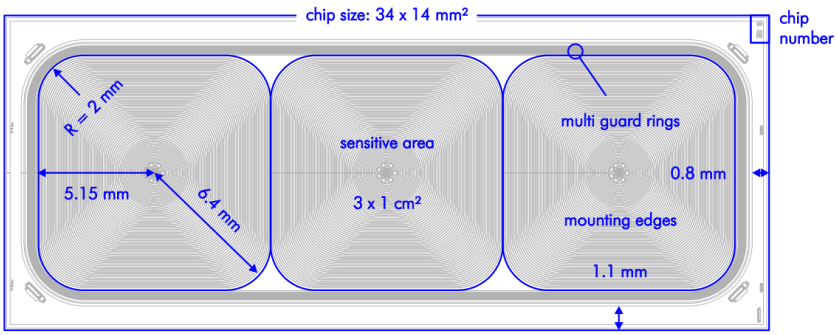

Figure 2.3: Front side of the SDD array of the VIP2 experiment [5].

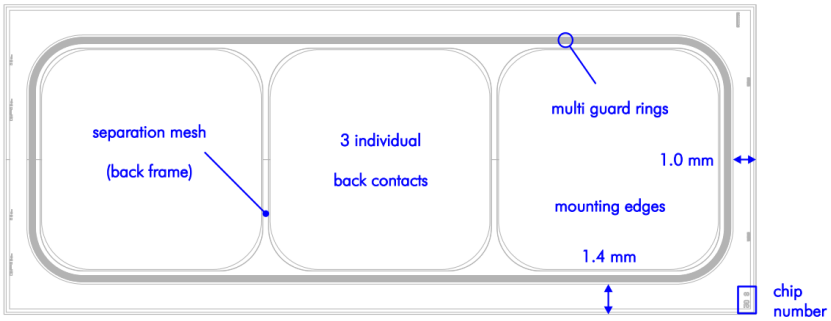

Figure 2.4: Back side of the SDD array of the VIP2 experiment. X-rays are incoming from this side [5].

The time resolution of the SDDs is determined by the drift time of the electrons from their origin to the anode. In [7] the maximum drift time at 150 K for the type of detector used in the VIP2 experiment is estimated to be 800 ns. Due to the temperature dependence of the electron mobility, the time resolution generally deteriorates with rising temperature.

2.2 Active Shielding

Its purpose is to reject SDD events caused by external radiation (e.g. from cosmic radiation). This means that whenever a signal in the SDDs coincides with a signal from the scintillators, it can be rejected. The active shielding consists of 32 scintillators read out by two Silicon Photomultipliers (SiPMs) each, which are assembled around the copper target and the SDDs. A render of the setup including the active shielding enclosing the target is shown in figure Figure 2.5.

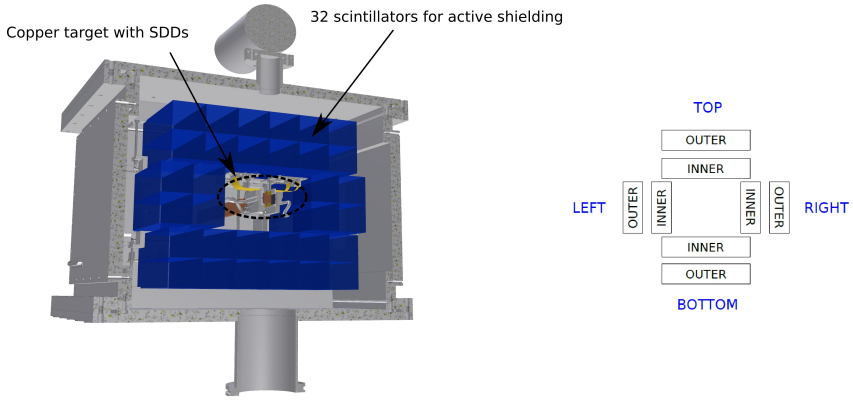

Figure 2.5: Render of the active shielding of the VIP2 experiment consisting of 32 scintillators (left). The scintillators can be grouped into an "outer" and an "inner" layer of 16 scintillators each (right) [5].

2.2.1 Scintillators

They are materials that emit photons after they are hit by ionizing radiation. The scintillators used in the VIP2 experiment are plastic scintillator bars with dimensions of 38 mm ×40 mm ×250 mm. When ionizing radiation passes through the scintillator, molecular orbits of the color centers are excited [9]. Subsequently the excited states loose their energy via the emission of a photon, typically in the UV range. To increase light collections on the SiPMs, the scintillators were wrapped in reflective aluminum foil to reflect stray photons back into the scintillator. To minimize the influence of photons from the environment (i.e ambient light) hitting the SiPMs, a layer of black tape was wrapped around the aluminum foil.

2.2.2 Silicon Photomultipliers

A Silicon Photomultiplier consists of an array of semiconductor pn junctions working in reverse bias mode. On one end of each scintillator bar, two SiPMs are attached with optical glue and connected in series. As the probability of correlated dark counts in both SiPMs is suppressed compared to reading a single detector, the signal to noise ratio can be improved in this way. The energy of the optical photons from the scintillator (425 nm 2.9 eV) is enough to generate an electron-hole pair. The spectral response range for the SiPMs used for VIP2 is 350 nm - 900 nm [10], overlapping with the photon spectrum of the scintillator. The time resolution of a system of a scintillator read out by SiPMs is typically in the order of a few ns. This means that it is small compared to the time resolution of the SDDs, which is in the order of a few 100 ns.

2.3 Argon Cooling

The Silicon Drift Detectors used for the VIP2 experiment have a working temperature of around 150 K [7] or lower. To reach this temperature, a helium compressor coupled to a pulse-tube refrigerator is used with helium gas as a working medium. The cooling power produced by this system liquefies argon, which evaporates and cools the detectors down. After the pulse tube a thermal contact to the surroundings is installed. The pulse tube is suspended in a vacuum of 10^{-5} - 10^{-6} mbar. The working principle of this type of a refrigerator is shown in Figure 2.6.

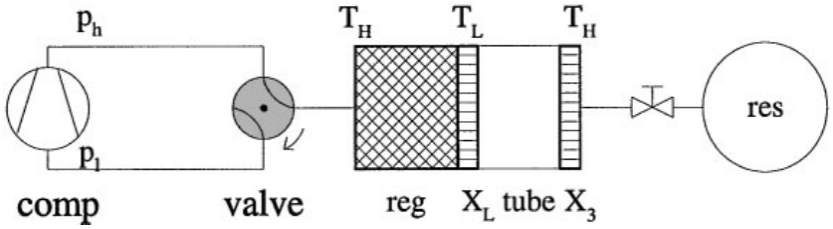

Figure 2.6: Schematic drawing of a pulse tube refrigerator [11].

The cooling power of the pulse tube refrigerator at X_L is used to cool down an aluminum volume through which the argon gas flows. The argon condensates and flows down a pipe which runs past the SDDs, cooling them to their working temperature. Thereby the argon evaporates. Afterwards it is cooled again by the pulse tube refrigerator. A picture of the SDDs with the argon cooling line and a readout board is shown in Figure 2.7

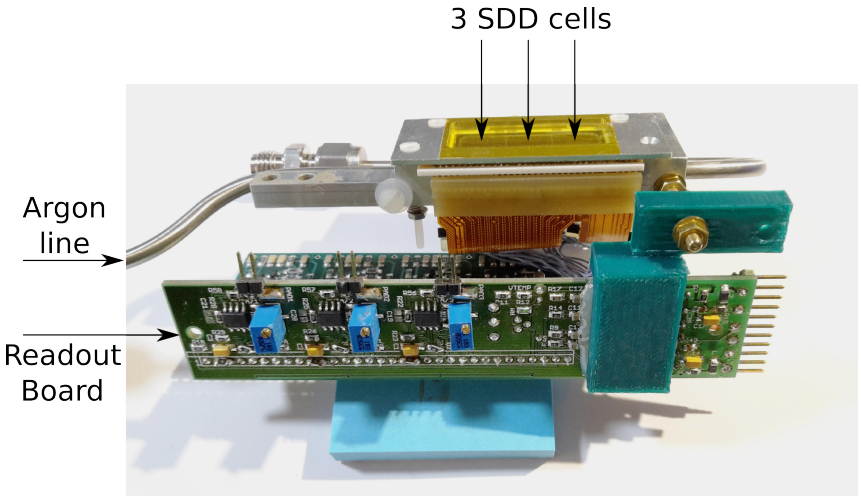

Figure 2.7: The SDDs with the argon cooling line and the readout board [5].

The cooling of the pulse tube refrigerator is counteracted by a heating wire controlled by a LakeShore 331 temperature controller. This is done in order to be able to control the temperature of the argon by adapting the heating power. Changes in argon temperature can in this way be compensated with the PID (Proportional Integral Differential) control of the LakeShore 331 on a very short timescale. The

vacuum needed to maintain the necessary cryogenic temperatures is maintained by two turbo pumps connected to a common prepump. [5]

2.4 Slow Control System

The slow control system is a system which monitors and controls important parameters of the experiment. A schematic drawing of its layout is shown in Figure 2.8.

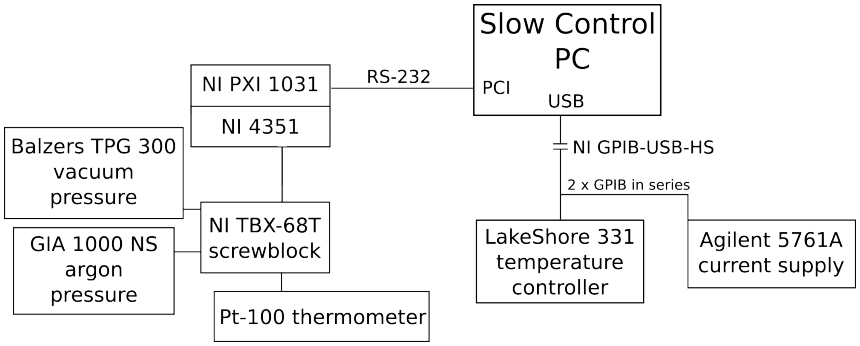

Figure 2.8: A schematic layout of the slow control system for the VIP2 experiment [5].

The central point of the system is a PC running a Visual C++ program which communicates with the different sensors and devices via a GPIB-USB-HS interface, storing and manipulating values of different parameters. The PC can be accessed remotely to control parameters and transfer the stored data. On one hand the GPIB-USB-HS interface is connected to a temperature controller which regulates the heating of a resistor which counteracts the cooling of the cold head and thereby regulates the argon temperature. On the other hand, the interface is connected to a current supply which provides the current through the copper target. The PC is also connected to a PXI-chassis with a PXI-board. This is then connected via a flat ribbon cable to a screwblock which receives analog signals from several sources, which correspond to pressure and temperature at different points in the setup. Temperature information comes from PT-100 resistance thermometers and pressure readings come from a cold cathode gauge for vacuum pressure (on the order of 10^{-5} mbar) and pressure sensors, made of a material that changes under mechanical strain (piezoresistive), for the pressure of the argon gas (on the order of 1 bar). An emergency system is in place which periodically checks the values recorded by the slow control system. If case specific values (like vacuum pressure and SDD temperature) exceed set thresholds, crucial systems like the turbomolecular pumps and the SDDs are turned off automatically [5].

Chapter 3

Proposed Improvements and Experimental Realization

3.1 Proposed improvements

Following the description of the experimental setup further improvements to enhance the signal and reduce the background in the energy region of the forbidden transition were proposed. To reduce the background, it is important to shield the detector from high energy photon radiation. This will be done by a passive shielding consisting of two parts. An outer part, 5 cm in thickness, made of low radioactivity lead and an inner part which is 5 cm in thickness, made of low radioactivity copper. Both parts will completely enclose the setup. The inner copper part rests on a frame constructed from Bosch profiles. Furthermore, a Teflon shielding of approximately 5 mm thickness inside of the experimental setup around the copper target and the silicon detectors can be applied to increase the passive shielding from the outside photon radiation in the energy region of the non-Paulian X-ray transition at 8 keV [12].

Another fundamental part of the proposed optimization is the implementation of new SDDs [13]. These new detectors were developed in a cooperation between Fondazione Bruno Kessler (FBK), Politecnico di Milano and SMI. They consist of units of 9 single cells of 8×8 mm^2, assembled in a 3×3 matrix with a fraction of active area as high as 85%. A picture of the SDD unit is shown in Figure 3.1. Four of the SDD units will be used, with two on each side of the target. With one cell having a surface area of 64 mm^2, the total active area will be of around 23 cm^2, i.e. about four times the current active area of 6 cm^2. Another advantage is that this type of detector can be operated at higher temperatures of around 230 K. The currently used SDDs are operated at about 100 K and require argon cooling. The higher operating temperature can be provided by Peltier cooling, which is better suited for long term data taking because of its stable and failure-free operation. The setup for Peltier cooling and signal readout of the SDDs is displayed in Figure 3.1, Figure 3.2 and Figure 3.3 [12].

A ceramic board for the SDD voltage supply and the read-out is mounted on the side of the SDDs opposite to the radiation entrance windows. The first stage of preamplification is provided by a new preamplifier (CUBE), which was recently developed by Politecnico di Milano. These preamplifiers allow high performance X-ray spectroscopy with standard SDD technology. The ceramic board is connected

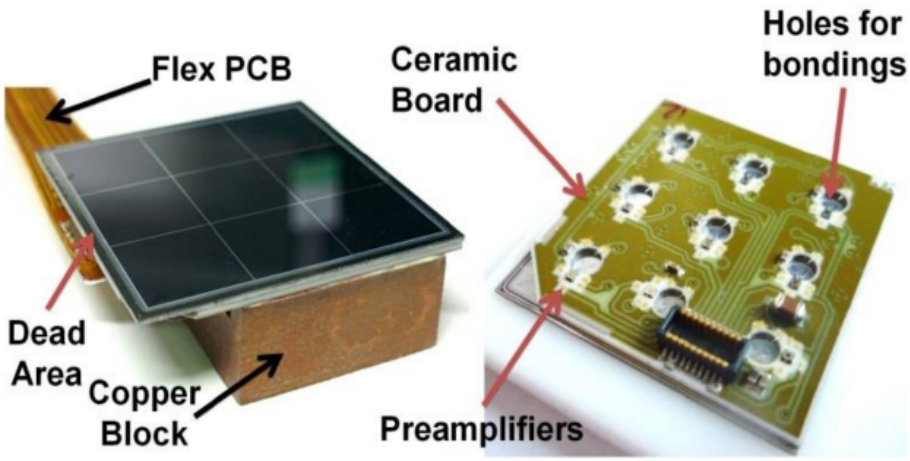

Figure 3.1: New type of SDD with ceramic board for contacting and readout and copper block for cooling [12].

to a readout board for further amplification and data acquisition. On the backside of the ceramic board a copper block is mounted which is attached to the cold side of a Peltier element. This attachment will be realized in the upgraded setup by a thermally conductive copper strip (Figure 3.2). It is via this copper strip, that the SDD is cooled by the Peltier element. The warm side of the Peltier element is cooled by a closed water cycle with a cooling pump. A similar water cooling is currently in use to cool the copper target. This system can be adapted to cool the Peltier elements in addition to the copper target [12].

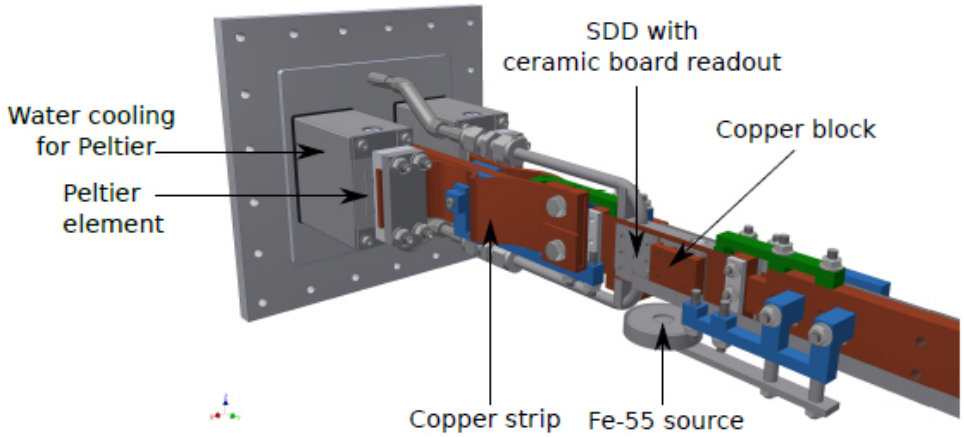

Figure 3.2: Render of the upgraded setup: The Peltier element is attached to a copper block, which is attached to backside of the ceramic board, with a copper strap. The Fe-55 source for energy calibration is shown. Some parts of the setup are not displayed to enhance the visibility [12].

In order to reduce the background coming from radioactive radon, the whole setup, including the passive shielding, will be enclosed in an existing plastic box where nitrogen is flushed. This Radon Reduction System (RRS) reduces the radon concentration in the atmosphere surrounding the experiment. Radon is an important

source of background at LNGS, as it is part of the decay chains of uranium and thorium, which in turn are abundant in the rocks of the Gran Sasso mountains [12].

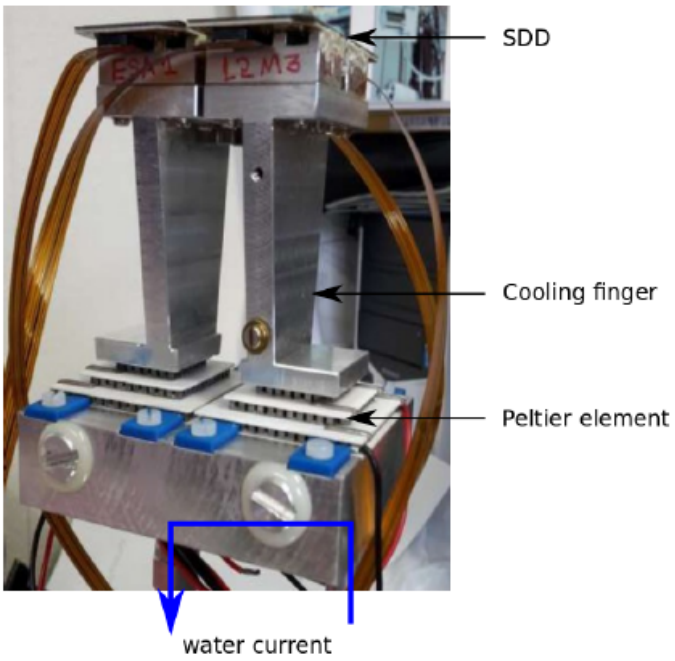

Figure 3.3: Test setup of SDDs with 3-stage Peltier cooling (bottom), cooling finger (middle) and SDDs (top) [12].

In the upcoming sections the experimental realization of the proposed improvements will be explained, along with some additional changes that might happen along the way due to results suggesting that another method or approach might be more suitable to be used in our case.

3.2 Tests of the Active Shielding

Taking into consideration that the VIP-2's active shielding has been consistently used for approximately three years, a long overdue quality check was executed. The shielding consists of 32 scintillators that are read out by two Silicon Photomultipliers (SiPMs) each. Two measurements (with and without a radioactive source) were carried out on each of the 32 scintillators using small amplifier boards. Strontium-90 was used as the radioactive source for the majority of measurements along with a small, radioactive pocket watch (containing Radium-226) for the rest. The results of both measurements were compared and four different ratios, displaying the quality of the tested scintillators and SiPMs, have been established.

The first ratio correlates to "great" signal rates or a ratio of approximately 100:1 between the count rates measured with a radioactive source (red curve) and the measured background count rates (black curve). An example of this is shown in Figure 3.4.

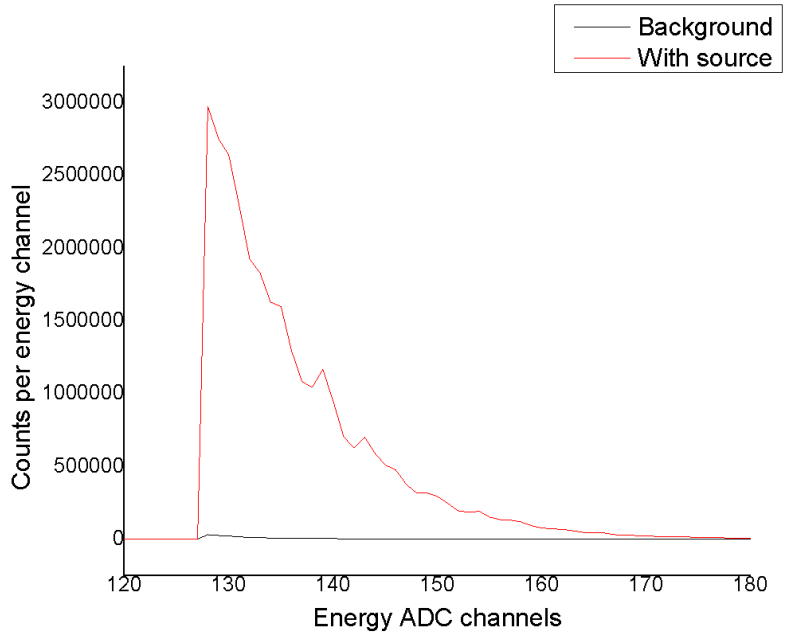

Figure 3.4: Great signal rates using scintillator-10 SiPM-1.

The second ratio of approximately 50:1 represents "good" signal rates between the count rates measured with a radioactive source (red curve) and the measured background count rates (black curve). e.g. Figure 3.5.

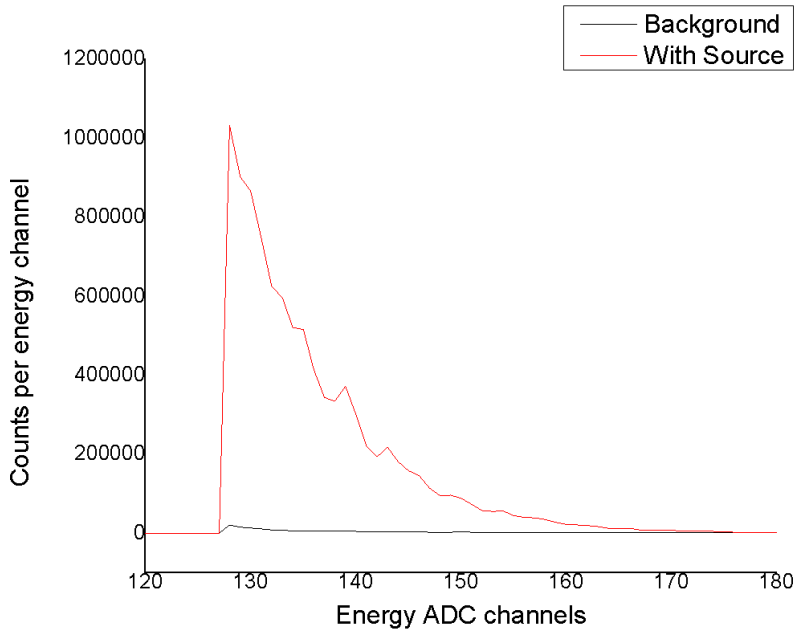

Figure 3.5: Good signal rates using scintillator-24 SiPM-2.

The third ratio correlates to "bad" signal rates or a ratio of approximately 15:1 between the count rates measured with a radioactive source (red curve) and the measured background count rates (black curve). In Figure 3.6 an example of this can be found.

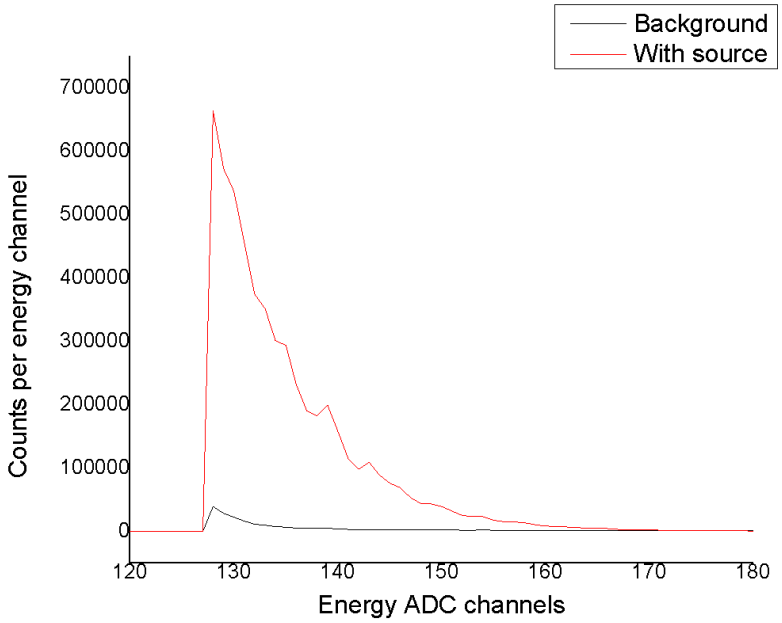

Figure 3.6: Bad signal rates using scintillator-25 SiPM-1.

The final (fourth) ratio of approximately 1.5:1 represents almost identical signal ratios between measurements with (red curve) and without (black curve) a radioactive source. An example of this is shown in Figure 3.7.

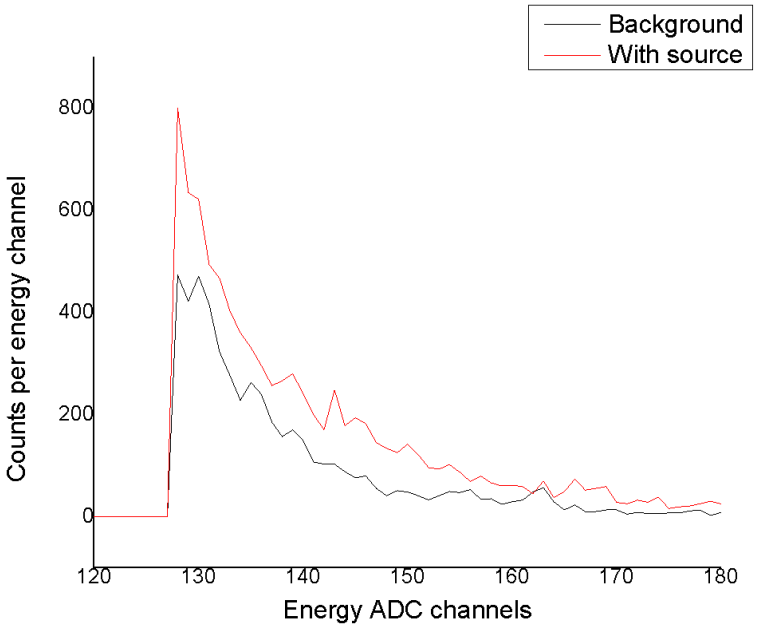

Figure 3.7: Almost identical signal rates using scintillator-30 SiPM-1/2.

A lot of different reason could be causing some of those scintillators and SiPMs to stop working properly, which is why all of those with "bad" and/or "identical" signal rates are getting fixed or replaced. In Table 3.1 a list of those SiPMs is shown.

Out of 32 scintillators used, where each is being read out by two Silicon Photomultipliers, almost a third of them were not working properly. This means that

SiPM	Result
$8-2$	almost identical signal rates
$9-2$	bad signal rates
$15-14$	almost identical signal rates
$16-24$	bad signal rates
$16-36$	bad signal rates
$19-1$	almost identical signal rates
$19-2$	almost identical signal rates
$23-2$	bad signal rates
$25-1$	bad signal rates
$25-2$	bad signal rates
$30-1/2$	almost identical signal rates

Table 3.1: List of all ineffective SiPMs that need to be fixed or replaced.

some or maybe even all of the SiPMs used had to be replaced.

While the active shielding is being repaired or upgraded (both equally likely) we decided to use a passive shielding instead to start our measurements.

3.3 Peltier Cooling

The overall upgrade of the experimental setup meant a change in the VIP-2's cooling. As a consequence, three stage thermoelectric peltier coolers were planned to be used for cooling down the SDDs instead of the previously used liquid Argon cooling. Thermoelectric coolers operate according to the Peltier effect. This effect creates a temperature difference by transferring heat between two electrical junctions. A voltage is applied across joined conductors to create an electric current. When the current flows through the junctions of the two conductors, heat is removed at one junction and cooling occurs, while on the other junction heat is deposited. In Figure 3.8 and example of such a three stage thermoelectric peltier cooler is shown.

Figure 3.8: Three stage peltier cooler.

3.3.1 First measurements using a peltier cooler

The first step was to run a few measurements to test the three stage thermoelectric cooling itself. The peltier cooler was implemented within a small housing, which was put under vacuum. Sensitive temperature sensors (PT-100) were connected to the cooled Al-block on opposing sides (two PT-100 sensors), in addition to a heater (which is used to simulate the heat dissipation of an SDD), and to the water cooled base (one PT-100 sensor). The cooled Al-block will be referred to as the "cold" side, while the water cooled base will be the "warm" side (Figure 3.9). Lastly, a current has to be applied to the peltier cooler.

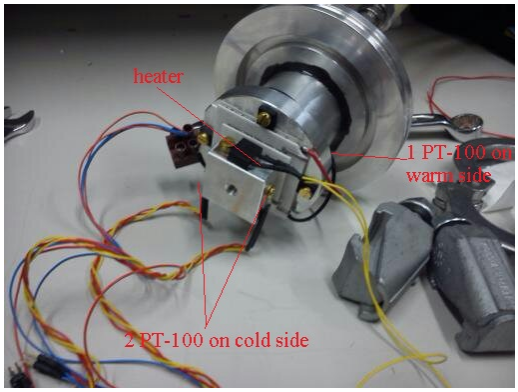

(a) PT-100 temperature sensors and a heater.

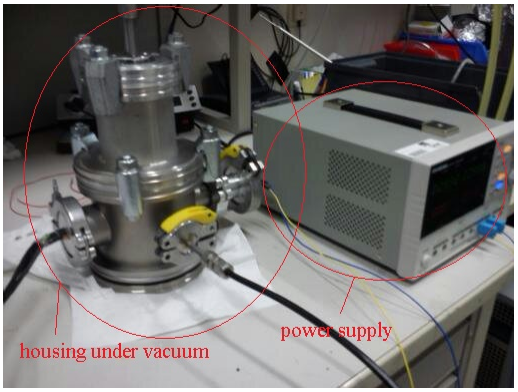

(b) Small vacuum housing and a power supply unit.

Figure 3.9: Measurement setup using a three stage thermoelectric peltier cooler.

This measurement involves testing how a current change from 3A to 1A, in 0.5A steps would affect the temperature on a cooled Al-block and a water cooled base without the heater being used. Following that, the next three measurements will use 0.5W, 0.75W and 1W of heating power. See Figure 3.10.

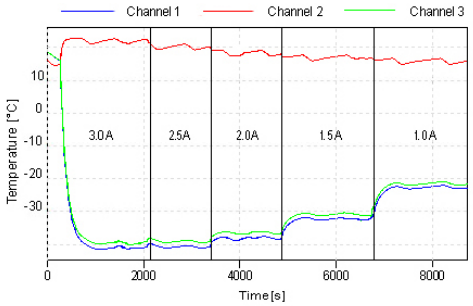

(a) Without heating

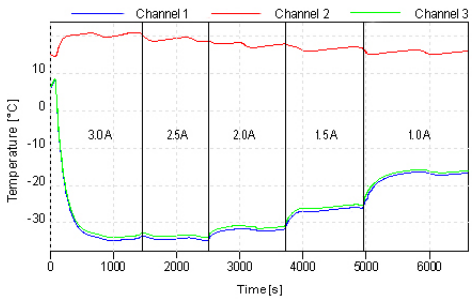

(b) 0.5 W

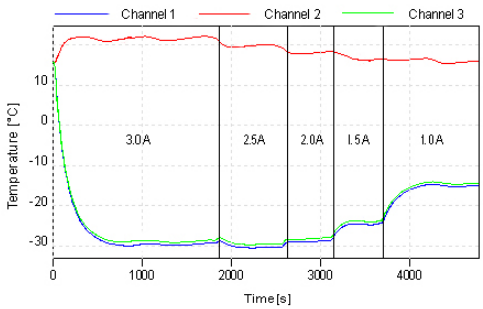

(c) 0.75 W

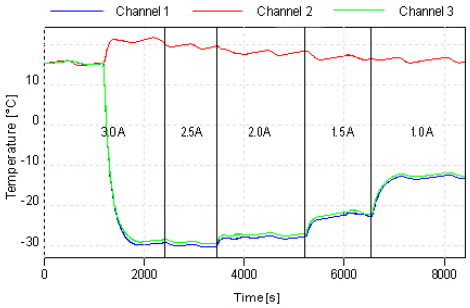

(d) 1 W

Figure 3.10: Measurement results using a peltier cooler with different heating powers including current changes. While using higher currents (> 1 A) our water cooling (Channel 2) was not capable of keeping the warm side of the Peltier cooler at a constant level, but it was slightly increasing it.

In Figure 3.10, Channels 1 and 3 correspond to the PT-100 sensors placed at the cold side of the peltier cooler and Channel 2 corresponds to the PT-100 sensor placed at the warm side of the peltier cooler. The dips in the graphs are explained by the change of current from 3A to 1A in 0.5A steps. In Table 3.2 the temperature values for each of those measurements can be seen.

			Current (A)				
			1	1.5	2	2.5	3
Without heater	Voltage (V)		4.25	6.1	8	10	11.7
	Temperature (°C) ±1° C	CH 1	−23	−32	−38	−41	−41
		CH 2	16	17	18	20	22
		CH 3	−22	−31	−37	−39	−39
With heater (0.5W)	Voltage (V)		4.17	6.1	8.02	10.15	11.7
	Temperature (°C) ±1° C	CH 1	−17	−26	−32	−35	−34
		CH 2	16	17	18	19	21
		CH 3	−16	−25	−31	−34	−33
With heater (0.75W)	Voltage (V)		4.21	6.12	8.06	10.3	12.7
	Temperature (°C) ±1° C	CH 1	−15	−24	−29	−29	−29
		CH 2	16	19	18	20	22
		CH 3	−14	−23	−28	−29	−29
With heater (1W)	Voltage (V)		4.19	6.1	8.1	10.26	12.3
	Temperature (°C) ±1° C	CH 1	−13	−23	−28	−30	−29
		CH 2	16	16	18	19	21
		CH 3	−13	−22	−27	−28	−28

Table 3.2: Temperature values reached during the first peltier cooler tests.

A more detailed look at the measurement results with and without the heater showed us that the temperatures reached were close to the value of around −40°C, which we need for cooling the SDDs to prove if Peltier cooling will be possible.

3.3.2 Second measurements using a peltier cooler

Following the results of the previous measurements, the peltier cooler was installed in a setup closer to the final one. Additionally, a copper braid similar to the one which is going to be used in the final setup is installed. In a similar fashion to the first peltier cooler measurements, one PT-100 was installed at the warm side of the peltier cooler, one at the cold side of it and one at the other end of the copper braid close to the heater (Figure 3.11).

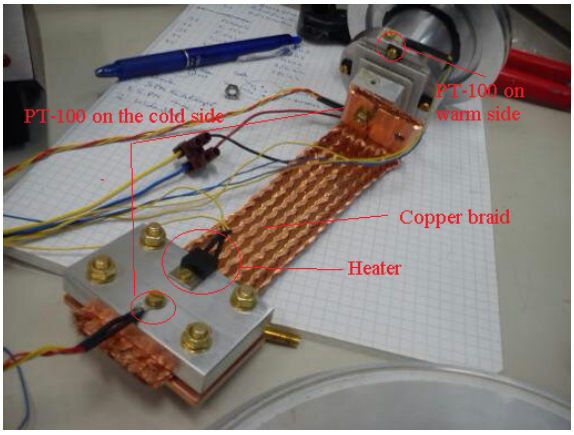

(a) Copper braid with PT-100 temperature sensors and a heater.

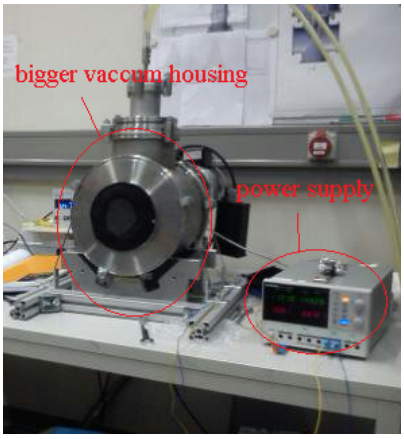

(b) Bigger vacuum housing and a power supply unit.

Figure 3.11: Measuring setup for the peltier cooler tests while using a copper braid.

Similar to the previous measurements the effects of the current change from 3A to 2A in 0.5A steps on to the thermoelectric peltier cooler and the thermal conductivity of the copper braid were measured. These measurements were performed without a heater. In the following graph the results of those measurements are shown (Figure 3.12).

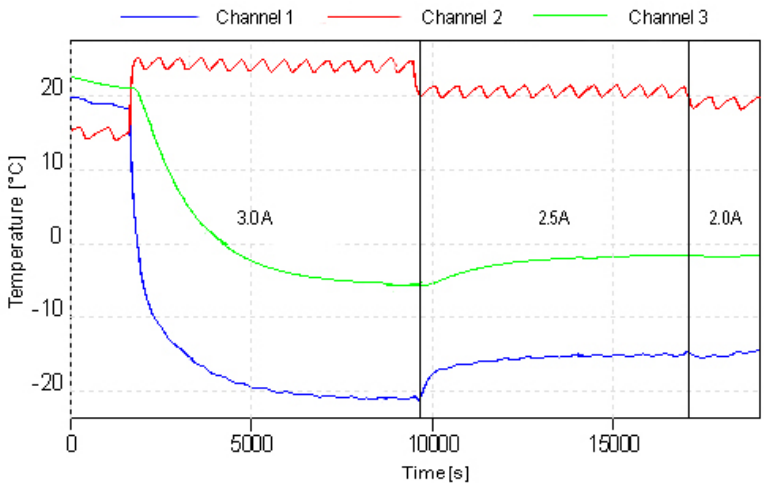

Figure 3.12: Results for the second peltier cooler tests while using a copper braid. The incapability to keep the warm side of the Peltier cooler at a constant level instead of it slightly increasing for higher currents can be observed particularly well in this case.

Channel 1 corresponds to the PT-100 sensor placed at the cold side of the peltier cooler, while Channel 3 corresponds to the PT-100 sensor placed at the other end of the copper braid and Channel 2 corresponds to the PT-100 sensor placed at the warm side of the peltier cooler. Taking a more detailed look at Table 3.3 reveals the temperature values reached during this measurement.

	Current (A)		2	2.5	3
Without heater	Voltage (V)		8.9	10.63	13.3
	Temperature (°C) ±1° C	CH 1	−14	−15	−21
		CH 2	20	21	25
		CH 3	−2	−2	−5

Table 3.3: Temperature values reached during the second peltier cooler tests.

This measurement shows that the thermal losses due to the copper braid were too high, considering that the temperature values reached were not sufficient for our experimental needs (about −40°C). Considering these non-satisfactory results, one of the reasons could be the lack of thermal contact between the peltier element's cold side (Al-block) and the copper braid. Another reason might have been that the weight of the copper braid had damaged the peltier cooler.

Taking both reasons into consideration, another measurement was prepared where the previous peltier cooler got replaced with an equal (but new) peltier cooler. In addition, a smaller copper braid has been used. Again, this measurement was executed without the heater simulating the heat dissipation of the SDDs. Figure 3.13 shows the measurement results, while in Table 3.4 the temperature values reached are shown.

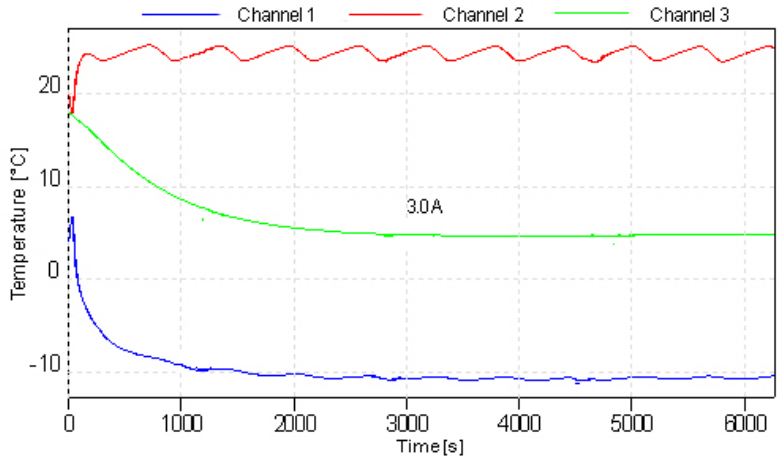

Figure 3.13: Measurement results for the new peltier cooler and the smaller copper braid. While using 3.0 A of current our water cooling (Channel 2) was not capable of keeping the warm side of the Peltier cooler at a constant level, but it was slightly increasing it.

	Current (A)		3
Without heater	Voltage (V)		14.93
	Temperature (°C) ±1° C	CH 1	−10
		CH 2	25
		CH 3	5

Table 3.4: Temperature values reached using the new peltier cooler and the smaller copper braid.

Taking a more detailed look at this result, the temperature values are significantly higher compared to the previous measurement, especially at the cold end of the peltier cooler (+10°C), even considering the lower thermal conductivity while using a smaller copper braid. This result may imply that some (if not all) of the PT-100 temperature sensors were malfunctioned as the cooled Al-Block should have reached a similar temperature value as in the previous measurement. Therefore a new, small setup will be used in addition to new PT-100 temperature sensors.

3.3.3 New measuring setup for the peltier cooler using aluminum alloys

The new setup for measuring the thermoelectric peltier cooler has a much smaller housing than the previously used setup in addition to new PT-100 temperature sensors, a heater and a smaller copper braid (Figure 3.15).

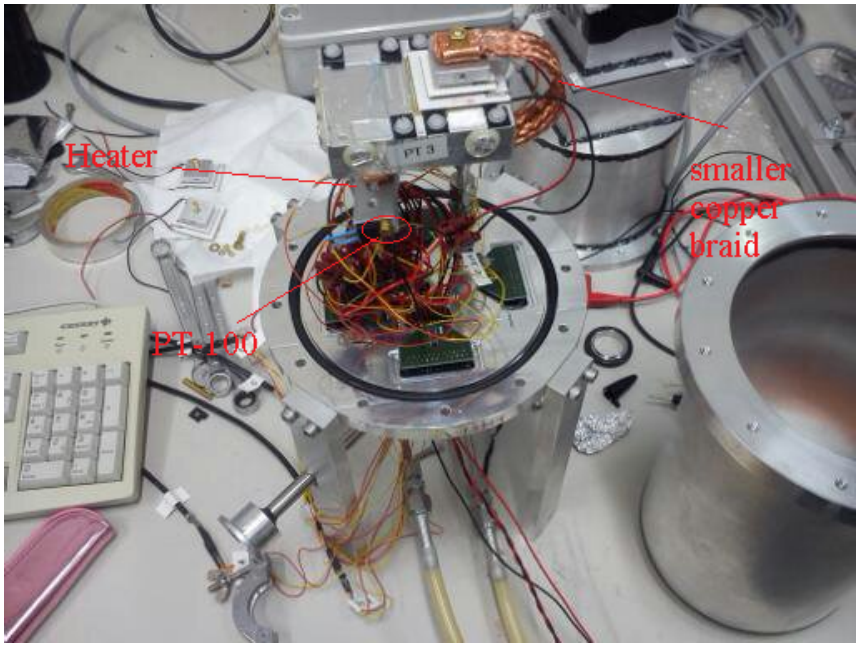

Figure 3.14: New peltier cooler setup with a smaller copper braid.

This measurement involves testing how a voltage change from 3V to 9V in 2V steps would affect the peltier cooler's performance and the thermal conductivity of the smaller copper braid. Furthermore, this measurement will be executed with 0.5W of heating power, simulating the heat dissipation of the SDDs. The results of these measurements can be seen in Figure 3.15.

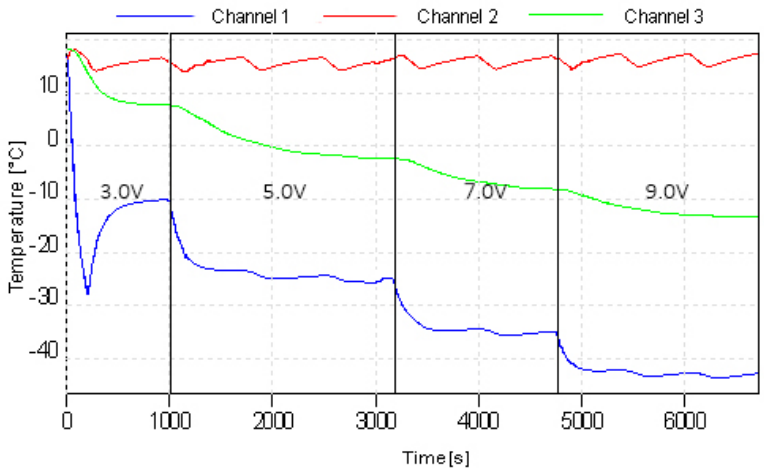

Figure 3.15: Results for the new setup with the smaller copper braid (for current values see Table 3.5).

In Table 3.5 the measured temperatures with the new setup using a smaller copper braid are shown.

	Current (A)		0.75	1.34	1.94	2.58
With heater (0.5W)	Voltage (V)		3	5	7	9
	Temperature (°C) ±1° C	CH 1	−10	−25	−35	−43
		CH 2	16	16	17	17
		CH 3	8	−2	−8	−13

Table 3.5: Temperature values reached using the new, small peltier cooling setup with the smaller copper braid.

Taking a more detailed look at these results, some improvements have been made with the measured temperature values at the cold side of the thermoelectric peltier cooler. An increase of approximately −20°C compared to the previous measurement shows promise. Unfortunately, the temperature values measured from the PT-100 temperature sensor placed on the other end of the smaller copper braid were still unsatisfactory.

A decision was made to try a solid bar made of aluminum to see if a better thermal contact can be reached compared to the copper braids. A pure aluminum stick (99.9999%) and aluminum alloys (AlCu, AlMgSi and AlPb) were used. Additionally, aluminum has only 60% of the thermal conductivity copper has, but its weight is much lower (Al density is 2.70 g/cm^3 while Cu density is 8.96 g/cm^3). Four measurements have been performed with 0.25W of heating power, simulating the heat dissipation of the SDDs. The results can be seen in the following graphs. (Figure 3.16)

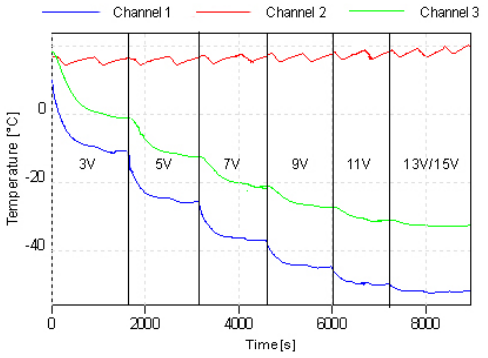

(a) AlCu (A = 0.6 cm^2, l = 20 cm)

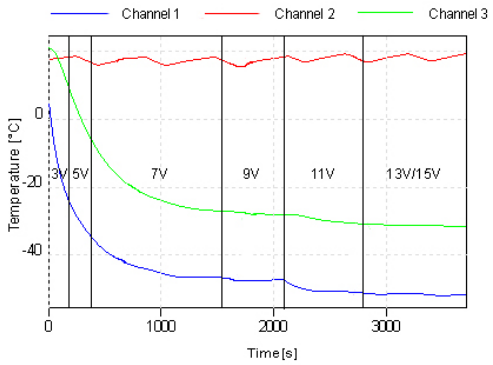

(b) AlMgSi (A = 0.6 cm^2, l = 20.25 cm)

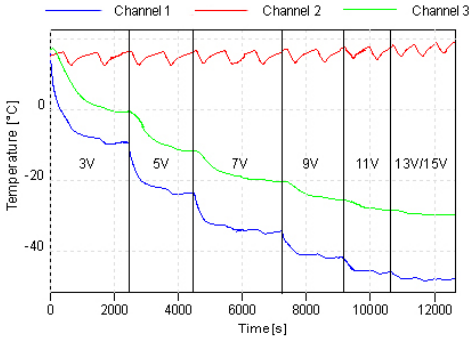

(c) AlPb (A = 1.5 cm^2, l = 19.8 cm)

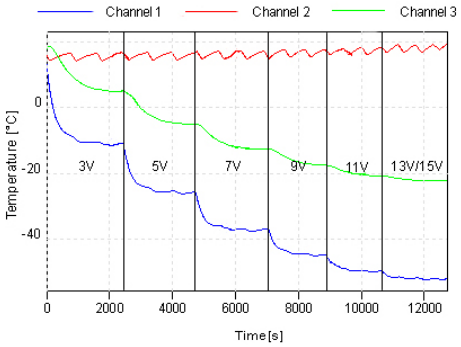

(d) 99.9999% (A = 0.2 cm^2, l = 14 cm)

Figure 3.16: Measurement results using one of either the pure aluminum stick or the aluminum alloys. "A" represents the surface area and "l" the length of either the aluminum stick or alloys.

Additionally, the heat (energy) flow values of the AlCu and AlMgSi alloys along with the pure aluminum stick were calculated from these results with 13 V of voltage used. These results can be seen in Table 3.6.

With heater (0.25W)	Thermal conductivity ~ 2W/cmK

	ΔT (K)	A/l (cm)	$\dot{Q}$ (W)	Losses (W)
AlCu	−19	0.030	1.15	0.90
AlMgSi	−20	0.029	1.19	0.94
99.9999%	−30	0.014	0.83	0.58

Table 3.6: Heat flow values using 13 V of voltage for the AlCu and AlMgSi alloys along with the pure aluminum stick. In this table $\dot{Q}$ represents the heat flow, A/l is the surface over length ratio and ΔT is the temperature difference measured between Channel 1 and Channel 3.

Taking a more detailed look at this table, we conclude that (assuming that the surface area used is doubled, as is the case with the AlCu and AlMgSi alloys) the pure aluminum stick would perform the best and have half of the ΔT value (temperature difference between Channel 1 and Channel 3) it has now.

Table 3.7 shows the results of the aluminum temperature measurements.

With heater (0.25W)			Voltage (V)						
			3	5	7	9	11	13	15
AlCu	Temperature (°C) ±1° C	CH 1	−11	−26	−37	−45	−50	−52	−52
		CH 2	16	16	17	17	18	18	19
		CH 3	−1	−12	−21	−27	−31	−33	−33
	Surface (cm^2) / Length (cm)		0.6/20						
AlMgSi	Temperature (°C) ±1° C	CH 1	−10	−25	−36	−44	−49	−51	−52
		CH 2	16	17	17	17	18	19	19
		CH 3	0	−11	−19	−25	−29	−31	−31
	Surface (cm^2) / Length (cm)		0.6/20.25						
AlPb	Temperature (°C) ±1° C	CH 1	−9	−23	−34	−42	−46	−48	−48
		CH 2	16	16	16	16	17	18	18
		CH 3	−1	−12	−20	−25	−28	−30	−30
	Surface (cm^2) / Length (cm)		1.5/19.8						
99.9999%	Temperature (°C) ±1° C	CH 1	−11	−26	−37	−45	−50	−52	−52
		CH 2	16	17	17	18	18	19	18
		CH 3	5	−5	−13	−18	−21	−22	−22
	Surface (cm^2) / Length (cm)		0.2/14						

Table 3.7: Temperature values reached using one of either the pure aluminum stick or the aluminum alloys.

This measurement shows improvements when it comes to the measured temperature values with the PT-100 temperature sensor placed at the other end of the aluminum stick/alloys (+(10−20)°C). The aluminum alloy AlCu (aluminum-copper) was the best performing one, reaching temperatures of approximately −33°C. Unfortunately, even AlCu's measured temperature values were not sufficient for our experimental needs of approximately −40°C. Moving forward the three stage thermoelectric peltier cooler will not be used for our main experiment and it will be replaced by a Polycold Compact Cooler (CryoTiger).

3.4 CryoTiger Cooling

Since our previous efforts of using a Peltier element were not satisfactory, a new cooling was required. The *Polycold Compact Cooler* (PCC) is a type of cryocooler manufactured by Brooks Automation, which is capable of reaching and maintaining temperatures as low as $-203°C$ (70K). The PCC cooling consists of basic modules: compressor, cryocooler and gas lines (Figure 3.17). The compressor continuously receives a low-pressure refrigerant from the cryocooler through the system return gas line. It compresses and cleans the gas, then delivers it through the system supply gas line to the cryocooler. The cryocooler receives a high-pressure, room-temperature refrigerant from the compressor via the supply gas line. As the gas flows through the heat exchanger, the supply refrigerant is cooled by the refrigerant returning from the cold tip of the cryocooler. The cooled refrigerant (with smaller droplets slowly forming) enters the throttle device, which allows the refrigerant to expand to a low pressure, thus cools the refrigerant faster, which enters the cold tip. Inside the cold tip the (now) liquefied refrigerant receives the user's heat load and starts evaporating before eventually leaving the cold tip at its final (cooled) refrigeration temperature at low pressure [14].

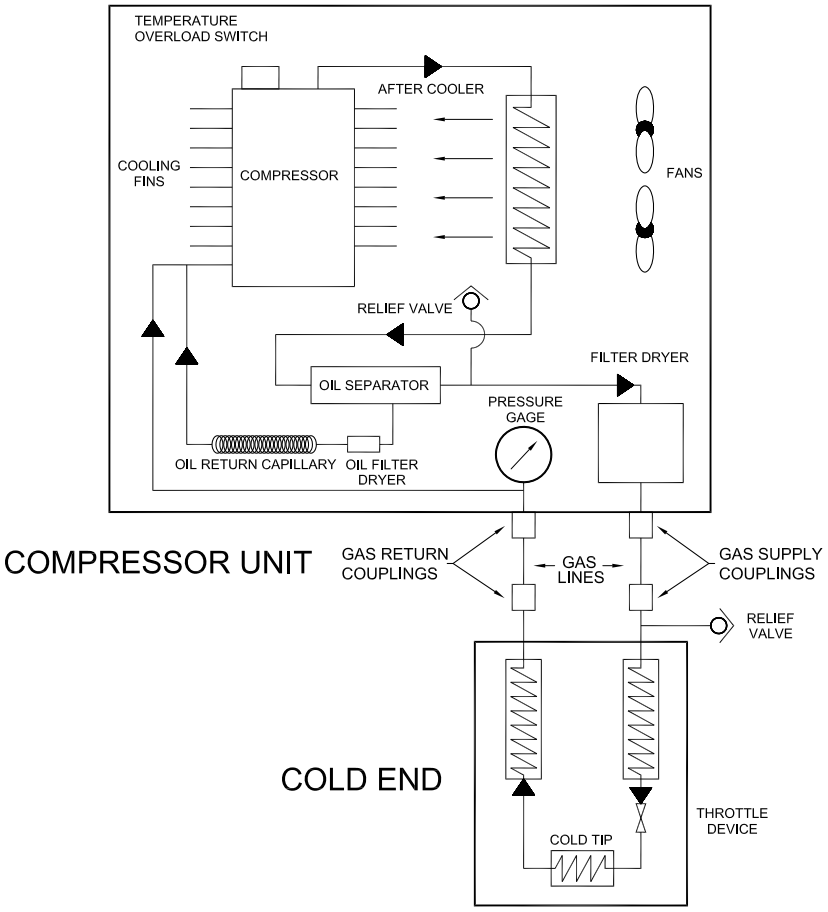

Figure 3.17: PCC Flow Diagram [14].

The measurement setup is installed in a vacuum chamber, which is created by a backing pump in conjunction with a turbomolecular pump (Figure 3.18). The main purpose of this is to prevent the formation of ice from water vapor in the air and to reduce heat conduction.

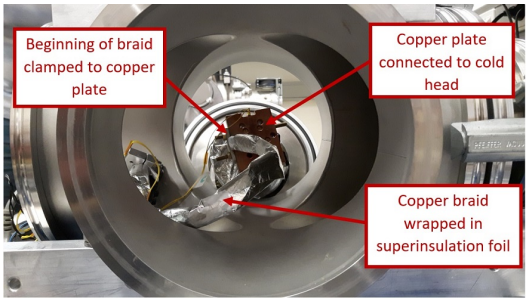

(a) Beginning of copper braid connected to cold head of PCC.

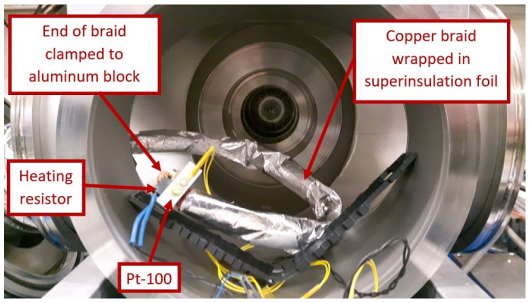

(b) End of copper braid with heating resistor simulating SDDs.

Figure 3.18: Measurement setup for PCC cooling with one copper braid installed [15].

To test the cooling performance, the cold head of the PCC was attached to a copper plate, with heat paste used to maximize thermal contact. One end ("cold end") of a heat conductor to be tested was clamped to the copper plate, using a smaller aluminum block, to which a PT-100 resistance thermometer was mounted. The other ("warm end") of this heat conductor was clamped inside a second aluminum block. A heating resistor, which simulated the power dissipation of an SDD array was attached to the latter aluminum block, as well as another PT-100 resistance thermometer.

The performance of the combination of different heat conductors and the PCC at transferring heat away from the resistor was measured. Taking the peltier element test results into account, the high-purity (99.999 %) aluminum rod (14 cm in length and 5 mm in diameter) will be further tested as a heat conductor in this measurement along with a copper braid (a copper strip made of individual copper wires braided together). Figure 3.19 and Figure 3.20 show the temperature curves as a function of time, for various powers used on the heat resistor. Those figures where the temperature rises instead of falling before it stabilizes correspond to measurements, in which the system was not cooled down from room temperature, but instead the heating power was increased from a previous measurement with lower heating power, without letting the system warm to room temperature first.

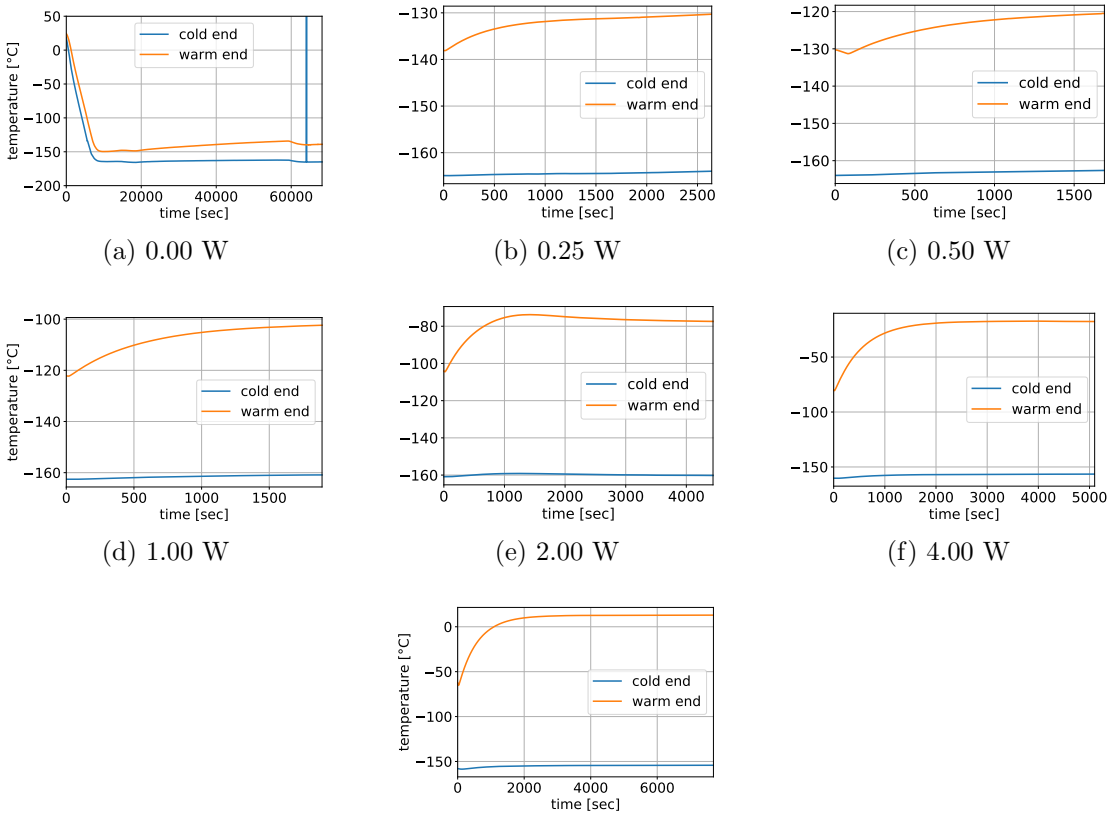

(a) 0.00 W (b) 0.25 W (c) 0.50 W

(d) 1.00 W (e) 2.00 W (f) 4.00 W

(g) 5.00 W

Figure 3.19: High-purity aluminum rod, various heating powers [15].

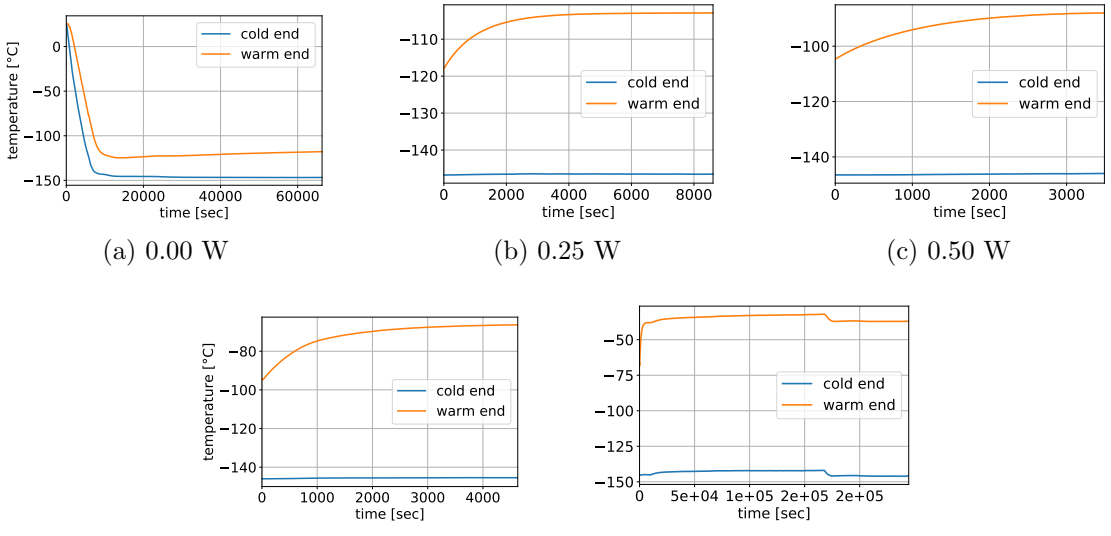

(a) 0.00 W (b) 0.25 W (c) 0.50 W

(d) 1.00 W (e) 1.50 W

Figure 3.20: One copper braid, various heating powers [15].

The spike shown in Figure 3.19 without any heating power used was due to a loose connecting wire. Additionally, a decrease around 60000 sec was noticed probably due to ambient air conditioning. Equivalent temperature drops can be seen in Figure 3.20 using 1.50 W of heating power, which was also believed to be an effect of the ambient air conditioning.

The final (approximately stable) temperatures that were achieved with the high purity aluminum rod and the copper braid are given in Table 3.8 and Table 3.9.

Power (W)	Warm end (°C)	ΔT (°C)
0.00	-139.008 ± 0.004	25.961 ± 0.007
0.25	-130.5 ± 0.1	33.6 ± 0.2
0.50	-120.7 ± 0.1	41.9 ± 0.2
1.00	-102.6 ± 0.1	58.3 ± 0.2
2.00	-77.35 ± 0.03	82.81 ± 0.05
4.00	-17.672 ± 0.006	138.83 ± 0.02
5.00	12.954 ± 0.004	167.19 ± 0.01

Table 3.8: High-purity aluminum rod. Final temperatures of the warm end and temperature differences ΔT between warm and cold end.

Power (W)	Warm end (°C)	ΔT (°C)
0.00	-117.97 ± 0.07	28.81 ± 0.08
0.25	-102.897 ± 0.002	43.625 ± 0.006
0.50	-88.03 ± 0.03	57.98 ± 0.05
1.00	-66.43 ± 0.06	79.01 ± 0.06
1.50	-36.85 ± 0.02	108.93 ± 0.04

Table 3.9: One copper braid. Final temperatures of the warm end and temperature differences ΔT between warm and cold end.

The values and the errors given were obtained by averaging over the last 250 sec of each measurement. However, the measurements were not always performed until temperatures were strictly stable, but, due to time constraints, often stopped as soon as the slope of the temperature had subjectively mostly leveled off. Additionally, there are many parameters to be controlled, including the ambient room temperature and the specifics of the interfaces between the different heat conducting components. Therefore, the final temperatures listed are only to be understood as rough estimates. They should, however, allow an estimate as to whether the PCC cooling is viable or not.

These measurements confirm the assumption that the thermal heat flow of the copper braid is not as good as that of the high-purity aluminum rod with almost the same A/l ratio, which achieved $20 - 30$°C lower temperatures on the warm side (where the heating resistor is located). The copper braid, however, has the advantage of being flexible, which makes it easier to install.

Additionally, the heat (energy) flow values using different heater powers for the high-purity aluminum rod were calculated from these results. These results can be seen in Table 3.10.

A/l (0.014cm)	Thermal conductivity $\sim$ 2W/cmK

Power (W)	ΔT (K)	$\dot{Q}$ (W)	Losses (W)
0.00	26	0.73	0.73
0.25	34	0.94	0.69
0.50	42	1.17	0.67
1.00	58	1.63	0.63

Table 3.10: Heat flow values using different heating powers for the high-purity aluminum rod. In this table $\dot{Q}$ represents the heat flow, A/l is the surface over length ratio and ΔT is the temperature difference measured between the warm and cold end.

If we compare this result using 0.25 W of heating power, with the PCC, to the result of a similar measurement with the peltier cooler (Table 3.6 we can see that the losses slightly increased. Considering that the losses are consistently increasing with more heating power, these results would suggest that perhaps the thermal contact with the heater or maybe even the heater itself was faulty.

Furthermore, an additional measurement was taken to test the limits of the PCC's cooling performance by installing an identical second copper braid (including a heating resistor on the other end of the braid) beside the first one. Figure 3.21 shows the temperature curves as a function of time, for various powers used on the heating resistor, while the results from this measurement are displayed in Table 3.11. Interestingly enough, the warm ends of the two copper braids exhibit a notable difference in temperature in the order of 10°C, although they are identical and both heating resistors were operated at the same power.

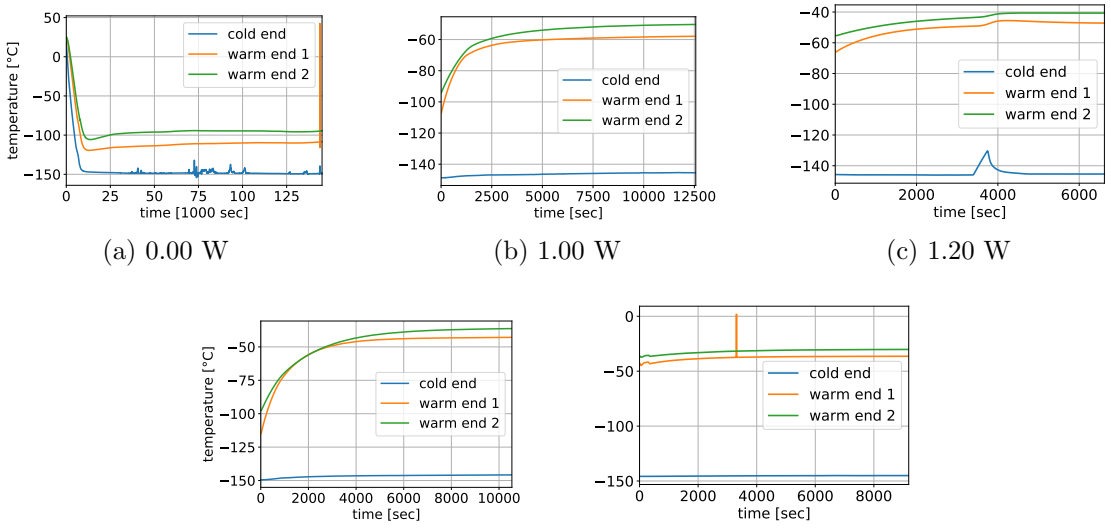

(a) 0.00 W (b) 1.00 W (c) 1.20 W

(d) 1.30 W (e) 1.40 W

Figure 3.21: Temperature curves for two copper braids, for various heating powers [15].

Power (W)	Warm end 1 (°C)	ΔT_1 (°C)	Warm end 2 (°C)	ΔT_2 (°C)
0.00	-108.7 ± 0.5	40 ± 1	-94.8 ± 0.2	54 ± 0.8
1.00	-58.1 ± 0.1	87.4 ± 0.2	-50.5 ± 0.2	94.9 ± 0.2
1.20	-47.17 ± 0.02	98.24 ± 0.03	-40.68 ± 0.002	104.726 ± 0.008
1.30	-42.883 ± 0.009	102.91 ± 0.02	-36.33 ± 0.02	109.47 ± 0.03
1.40	-36.404 ± 0.004	108.666 ± 0.007	-30.194 ± 0.005	114.877 ± 0.007

Table 3.11: Two copper braids simultaneously. Final temperatures of the two warm ends and temperature differences ΔT between warm and cold end.

Taking a more detailed look at Figure 3.21 without any heating power (the powers given are those at which both heating resistors were operated individually) used, the fluctuations in the temperature at the cold end are likely due to a faulty wire, which was repaired before continuing the measurements. While using 1.20 W of heating power a temperature increase was noticed due to the cryocooler's power supply becoming temporarily disconnected. Furthermore, at 1.40 W of heating power a temperature spike was noticed likely due to a connection wire being tugged.

Finally, the results suggest that the PCC is capable of delivering the needed low temperatures (even in the long term). Even in the last measurement with two separate heating resistors connected to the cold head via individual copper braids, the temperatures on the warm ends remained comfortably below -35°C for heating powers up to 1.20 W (on both heating resistors individually), which is greater than the expected heat dissipation of an SDD array.

3.5 New Silicon Drift Detectors

3.5.1 Preamplifier tests

Another task carried out was testing a type of preamplifier for reading out the output signal of 3×3 SDDs arrays (Figure 3.22). More specifically, the linearity of the preamplifier is of interest. Both this preamplifier and the 3×3 SDD arrays are different from those currently planned to be used in the final VIP2 setup. The difference, however, only concerns the number of channels and some secondary features, and not the basic functioning of the amplifier. Therefore, testing the linearity of this type of preamplifier may still be useful in view of the one envisaged for use with the other SDD arrays in the final measurement setup.

Three channels, labeled 1, 3 and 8, of the preamplifier (Figure 3.22) were tested.

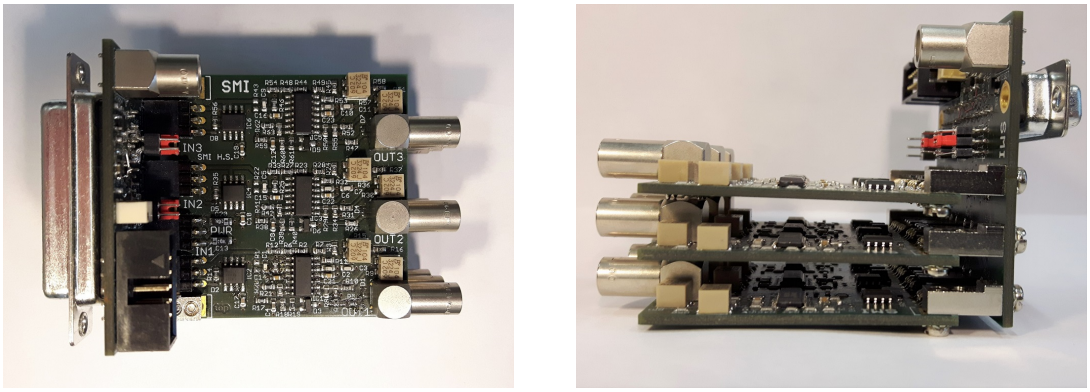

Figure 3.22: Preamplifier, top and side view [15].

Input signals from a BNC Model PB-4 pulse generator, operated in *tail pulse* mode, were fed into the preamplifier. The maxima of input and output voltages were recorded on a LeCroy WaveRunner 625Zi oscilloscope, for a number of input voltages varying between about 5 and 40 mV. To estimate statistical errors on the measured voltages (input as well as output), over 500 recorded events (i.e., pulses) were averaged for each individual input voltage. From this data, the supposed linear relation between input and output voltages was inferred using orthogonal distance regression. The results are presented in Table 3.12.

Channel number	Slope	Intercept (mV)
1	10.72 ± 0.04	-32.1 ± 0.8
3	11.72 ± 0.09	-28 ± 2
8	11.19 ± 0.08	-24 ± 2

Table 3.12: Fit parameters characterizing linearity of preamplifier.

The gains (slopes) obtained in this way are not meaningful in an absolute sense, since the exact values depend on the measurement setup, specifically the input impedances. This should not, at least in principle, affect the linearity (or lack thereof). In Figure 3.23, the linear fit function is shown superimposed on the measured voltages, while Figure 3.24 shows the difference of the measured voltages to the fit.

These measured values show that the linearity of the three tested channels are within the necessary specification.

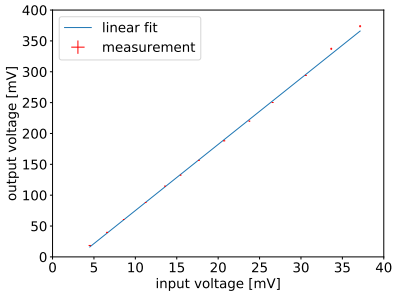

(a) Channel 1

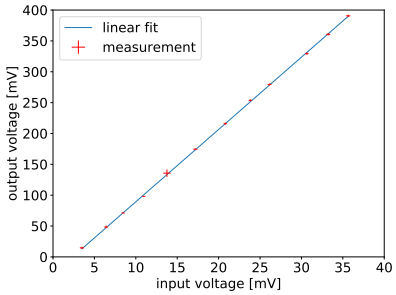

(b) Channel 3

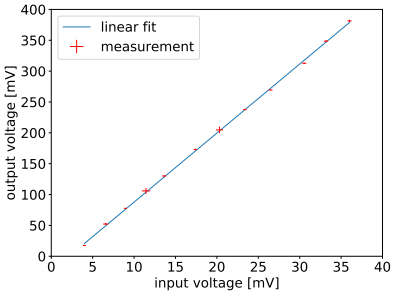

(c) Channel 8

Figure 3.23: Output voltages, plotted over input voltages, for three different channel of preamplifier. Linear fit functions are also shown. Error bars of measured data are included for both input and output voltages, however, they are barely visible since the errors are rather small [15].

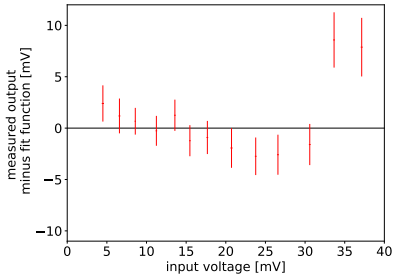

(a) Channel 1

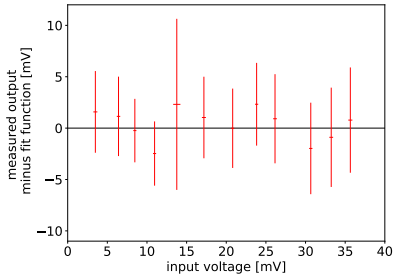

(b) Channel 3

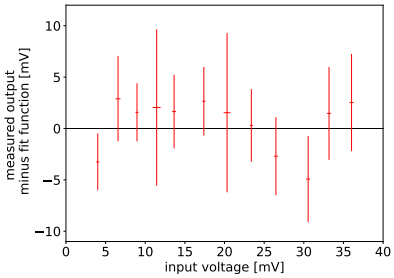

(c) Channel 8

Figure 3.24: Differences between measured output voltages of the preamplifier and values of the linear fit function. Error bars are included [15].

3.6 Newly developed SDD units

The SDDs used for the VIP2-Upgrade experiment use a complementary metal-oxide-semiconductor (CMOS) preamplifier, called CUBE, instead of the usually used JFET [16]. The CMOS is stationed on the ceramic support structure of the SDD array and is electrically connected to the anode. This essential difference, compared to SDDs with integrated JFET preamplifier, makes the new SDDs easier to fabricate, more stable and almost independent to small changes e.g. variations of the bias voltage and, additionally, the change from JFET to CMOS increases the latch-up performance of the new SDDs. The Ceramic Carrier is then screwed onto an aluminum block to keep the assembly stable and will be used for cooling [17]. Figure 3.25 shows the silicon wafer of the SDD array as well as the ceramic structure.

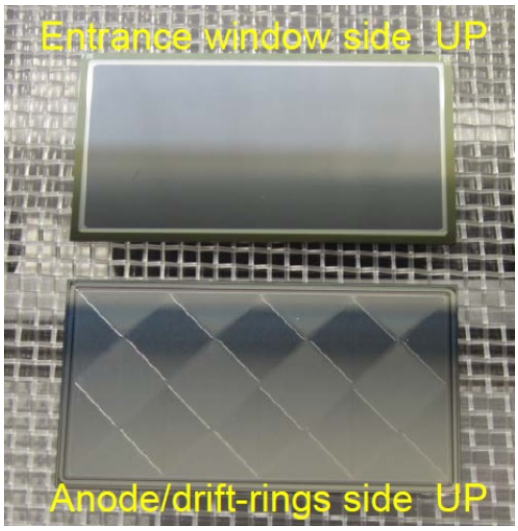

(a) View of the silicon wafer structure of one SDD array.

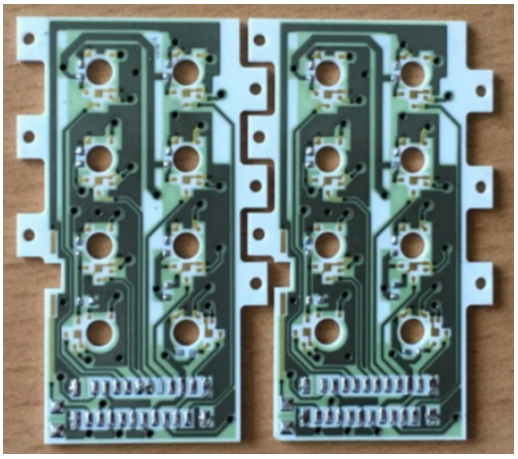

(b) View of the ceramic structure.

Figure 3.25: Silicon plate of one SDD array and back view of array.

One SDD array consists of 2×4 single SDD units. In the VIP2-Upgrade experiment 4 SDD arrays (meaning of 32 SDD cells) are needed. One SDD unit provides an active area of 8×8 mm^2. The individual SDD cells are divided by a thin potential well, minimizing crosstalk to under 1 % [17]. With only a margin of 1 mm on each side, the dead area of the SDD is dramatically reduced. A view of this is given in Figure 3.26. This increase in total active area is an important improvement of the detection efficiency compared to the previously used SDDs.

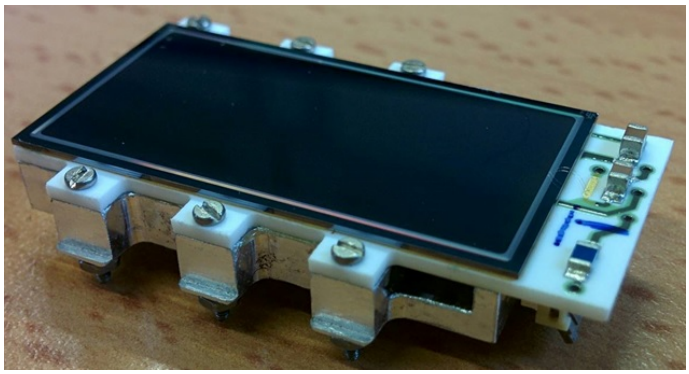

Figure 3.26: Single unit 4 × 2 SDD array.

3.6.1 Energy Calibration

The first calibration tests were performed in August 2015 with SDD array no. 5 with only four working channels CH2, CH6, CH7 and CH8. The temperature of the SDD array was at 168 K. As an X-ray source a Fe-55 source with an additional 5μm Ti foil was used to see four energy peaks, which can be used for energy calibration: Mn K_α, Mn K_β as well as Ti K_α and Ti K_β. The spectra were fitted with the same technique: The K_α peaks were fitted with two gaussian functions including the $K_{\alpha,1}$ and the $K_{\alpha,2}$ peaks using the same sigma but half the amplitude of $K_{\alpha,1}$ for the $K_{\alpha,2}$ peak, and with the mean shifted by the fixed eV value taken from [18]. For the two K_β peaks a single gaussian function was used. Additionally, the background was tuned to the best χ^2 with a cubic function. The full width half maximum (FWHM) of the Mn K_α peak was used as a reference value for the energy resolution.

The first measurement was taken with amplifier board 2.1 over 3 days [17]. The bias voltage was turned to the values $R_1 = -17.9$ V, $R_N = -91.0$ V and $R_B = -71.0$ V. The gate and reset thresholds as well as the ramp lengths for the well working four channels can be seen in Table 3.13.

Channel No.	Gate threshold (V)	Reset threshold (V)	Ramp (s)
2	0.08	2.12	2.5
6	0.15	2.52	1.8
7	0.06	2.04	7.0
8	0.08	2.53	1.2

Table 3.13: Amplifier Board and Voltage Settings for Version 2.1 [17].

Furthermore, a similar energy calibration test was performed in August 2018 with SDD no. 18. Data has been taken with a LeCroy WavePro 735Zi 3.5 GHz Oscilloscope using a Fe-55 source with an additional Ti foil. For the analysis, only the Mn K_α and K_β peaks were used [17]. Representative of this measurement, the calibration spectra of CH1 (cell 1) are shown in Figure 3.27. The measurement for the second spectra was performed a few days later and the Y-axis now includes a logarithmic scale.

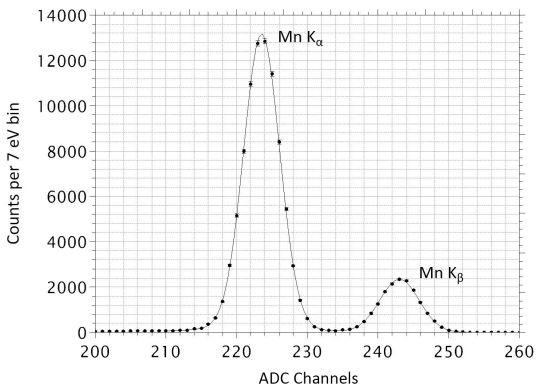

(a) Energy calibration of channel 1.

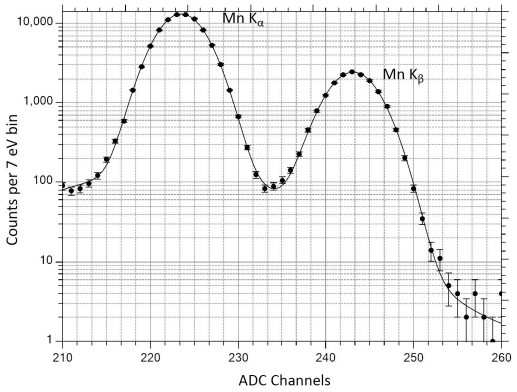

(b) Energy calibration of channel 1 with a logarithmic scale in the Y-axis.

Figure 3.27: Energy calibration spectra of CH1 (cell 1) of SDD no. 18. A single ADC channel corresponds to approximately 27 eV of energy.

Table 3.14 lists the amplitude, width, peak position and reduced chi-square values for the K_α as well as the K_β peaks for both spectra.

		Amplitude	Width	Peak position	Reduced chi-square
Normal spectrum	K_α	12975 ± 69	2.547 ± 0.009	223.54 ± 0.01	1.21
	K_β	2344 ± 28	2.77 ± 0.02	243.04 ± 0.03	
Spectrum with logarithmic scale on Y-axis	K_α	12961 ± 56	2.574 ± 0.008	223.532 ± 0.009	1.19
	K_β	2411 ± 24	2.67 ± 0.02	243.10 ± 0.02	

Table 3.14: Summary of energy calibration measurements for CH1 (cell 1) of SDD no. 18. The FWHM can be calculated by multiplying the width with 27 eV per ADC channel and a constant value of 2.35.

Additionally, this measurement shows that the differences between the measured values in both tests are almost negligible. The reduced chi-square values show that our analysis and thus the energy calibration itself is suitable for our measurements. Furthermore, this proves the operating stability of the SDDs used, as the measurement duration exceeded almost 24 hours in both tests.

3.7 New Slow Control System (LabVIEW)

In consideration of our cooling changes (among other) the old slow control system had to be adjusted accordingly. The new slow control system is programmed in a graphical programming language called LabVIEW. The LabVIEW program is supposed to measure, calculate and/or regulate temperature, pressure and current values, SDD high voltage, turbo pump and X-ray tube performances and send out warning messages if any of those components happen to malfunction or stop working.

For the purposes of this thesis work the LabVIEW program only focused on the temperature and pressure values considering that the other components were not needed for the preliminary measurements with the VIP2 experimental setup.

3.7.1 Brief introduction to LabVIEW

LabVIEW is a systems engineering software for applications that require testing, measurements, and control with rapid access to hardware and data insights. LabVIEW offers a graphical programming approach that helps visualize every aspect of the application, including hardware configuration, measurement data, and debugging. This visualization makes it simple to integrate measurement hardware from any vendor, represent complex logic on the diagram, develop data analysis algorithms, and design custom engineering user interfaces [19].

LabVIEW programs are called virtual instruments (VIs) where each VI contains three main parts:

- Front Panel – used for interacting with the user when the program is running.
- Block Diagram – shows the accompanying graphical source code for the front panel.
- Icon/Connector – means of connecting a VI to other VIs.

The Front Panel is the user interface of the VI. You build the front panel with controls and indicators, which are the interactive input and output terminals of the VI, respectively. Controls are knobs, push-buttons, dials, and other input devices. Indicators are graphs, LEDs, and other displays. Controls simulate instrument input devices and supply data to the block diagram of the VI. Indicators simulate instrument output devices and display data the block diagram acquires or generates.

The block diagram contains the graphical source code. Front panel objects appear as terminals on the block diagram. Additionally, the block diagram contains functions and structures from built-in LabVIEW VI libraries. Wires connect each of the nodes on the block diagram, including control and indicator terminals, functions, and structures.

3.7.2 LabVIEW Slow Control System

Front Panel

Figure 3.28 shows the front panel of the slow control system written in LabVIEW. It includes a Serial Port control, with which the COM-Port of the Arduino can be specified. Additionally, the File Path Control can be used to select the storage location for the log files. Clicking the STOP button ends the measurement gracefully. The Device Name shows the Arduino board used for the measurement. Furthermore, indicators for the calculated temperature and pressure values, along with their respective measured voltages are displayed to the left of the temperature and pressure charts.

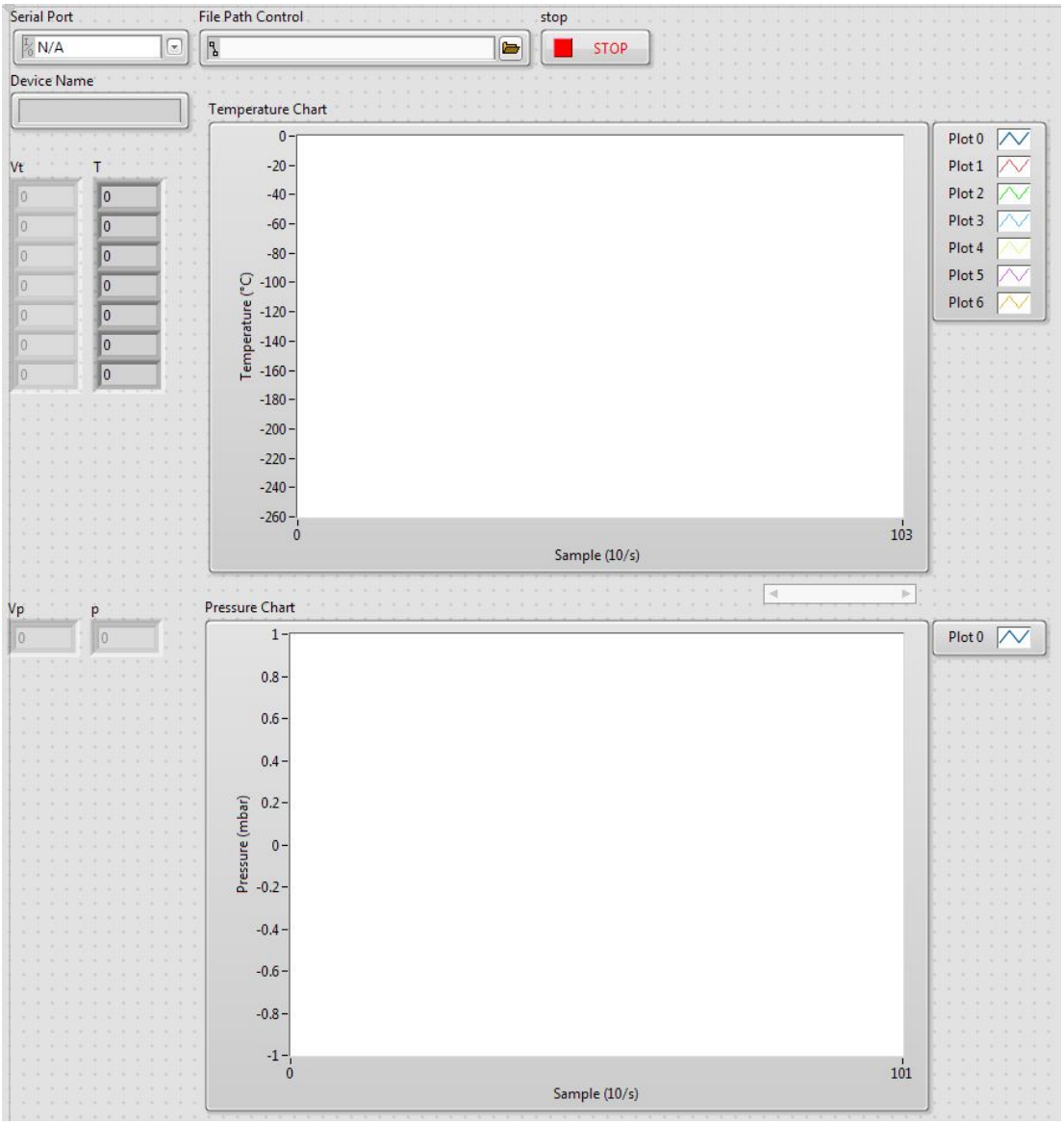

Figure 3.28: Slow control system's Front Panel used in the VIP2-Upgrade experiment.

Block Diagram

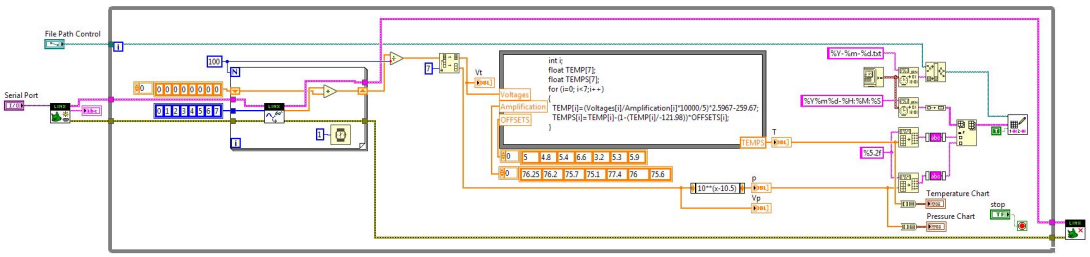

Figure 3.29: Overview of the slow control system's Block Diagram used in the VIP2-Upgrade experiment.

Taking a more detailed look at the block diagram, it was split into three separate sections. The first section (Figure 3.30) handles the initialization and opening the COM-port of the Arduino board and the log file storage path. The FOR loop is used to take 100 voltage measurements on Arduino Analog IN pins 0-7 using the analog read function of the LINX package, which are stored in an array and then used to calculate their mean values. Array indices 0-6 correspond to temperature values and index 7 corresponds to the pressure value.

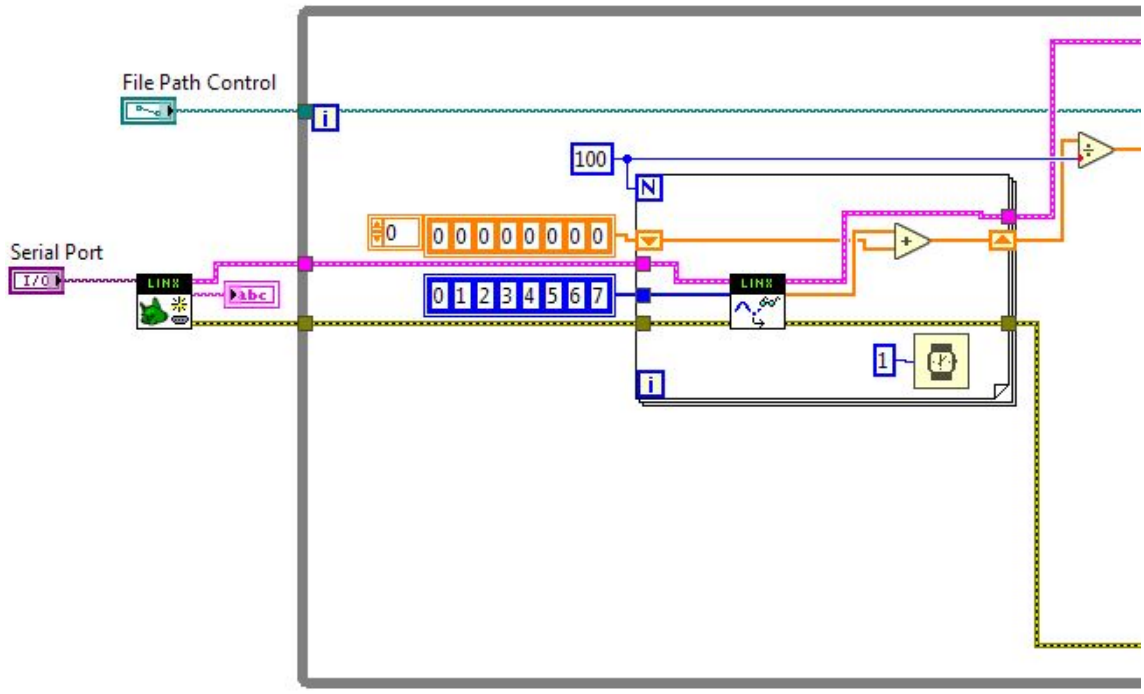

Figure 3.30: Section 1: Arduino initialization and data acquisition.

In the second section (Figure 3.31) the mean value of the measured voltage for pressure is being separated from the array and its value used for calculating the pressure. The rest of the array (indices 0-6) is used in combination with the amplification and offset arrays to calculate the temperatures in °C. The temperatures, the pressure and their respective voltages are relayed to the front panel indicators.

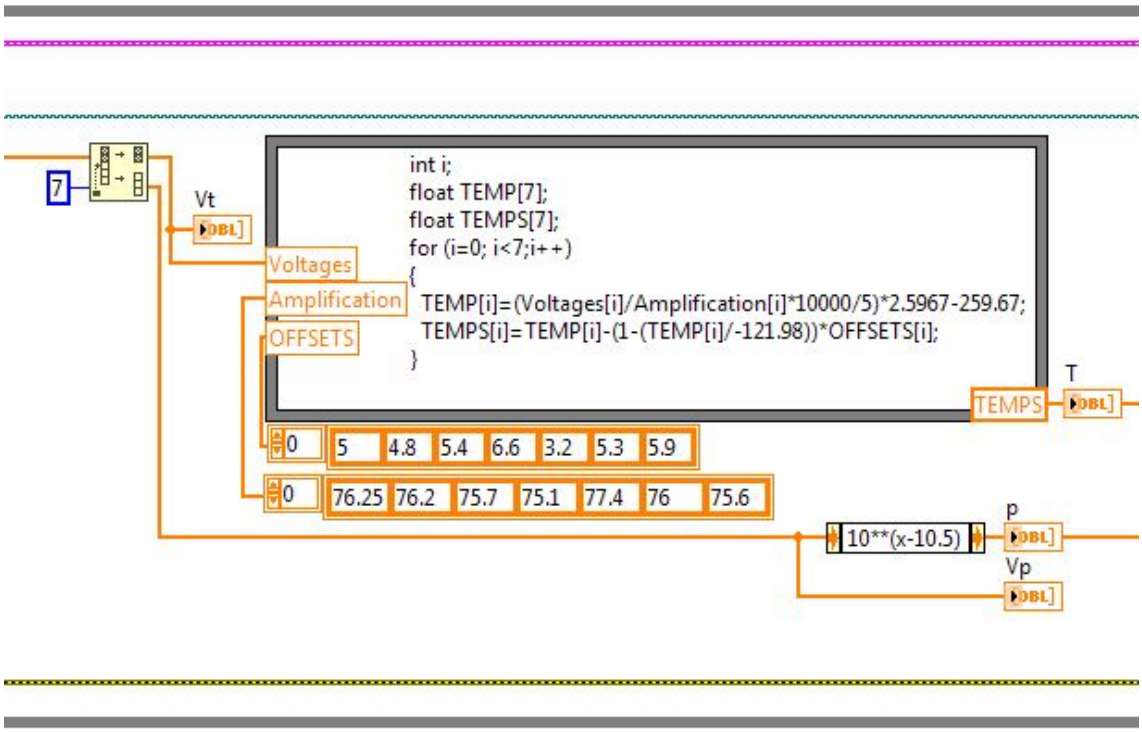

Figure 3.31: Section 2: Temperature and Pressure calculation from the measured voltages.

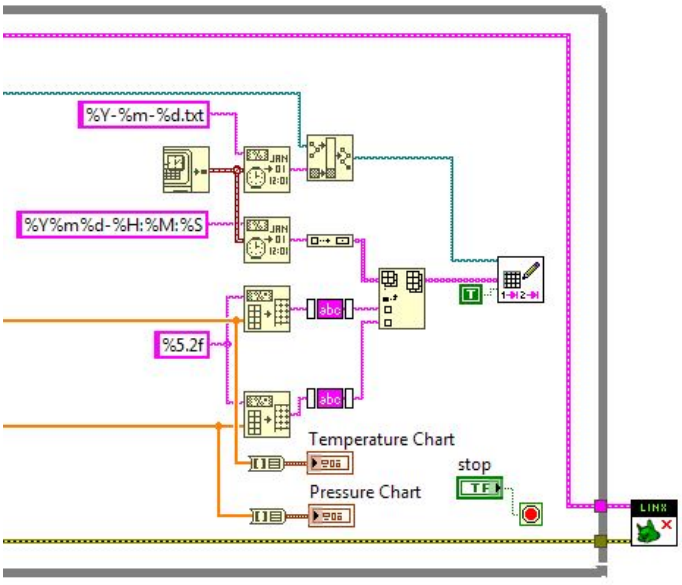

Figure 3.32: Section 3: Plotting, formatting and storing the data.

The last section (Figure 3.32) handles plotting the graphs as well as formatting the arrays into strings and saving the data into files. A new log file is created every day, its file name being the date of creation.

Chapter 4

Present Status of the VIP2-Upgrade Experimental Setup

The present status of the VIP-2 experimental setup follows from the results of all the individual tests for the proposed upgrade, including all the changes that were made along the way (see chapter 3). Instead of the active shielding (using scintillators and silicon photomultipliers), a passive shielding will be implemented instead. That is until the active shielding has been repaired or replaced. For the cooling, the Polycold Compact Cooler (CryoTiger) showed satisfactory results with low enough temperatures (less then $-50°C$) for ideal SDD performance. The new 2×4 SDDs with a bigger active area will be used, along with a slow control system for recording the temperature, for each PT-100 temperature sensor used, and pressure values. All the components will be combined inside a 55 cm $\times$40 cm $\times$32.8 cm vacuum chamber made out of 15 mm thick AlMg4,5Mn. In Figure 4.1 pictures of the vacuum chamber from the inside and outside can be seen.

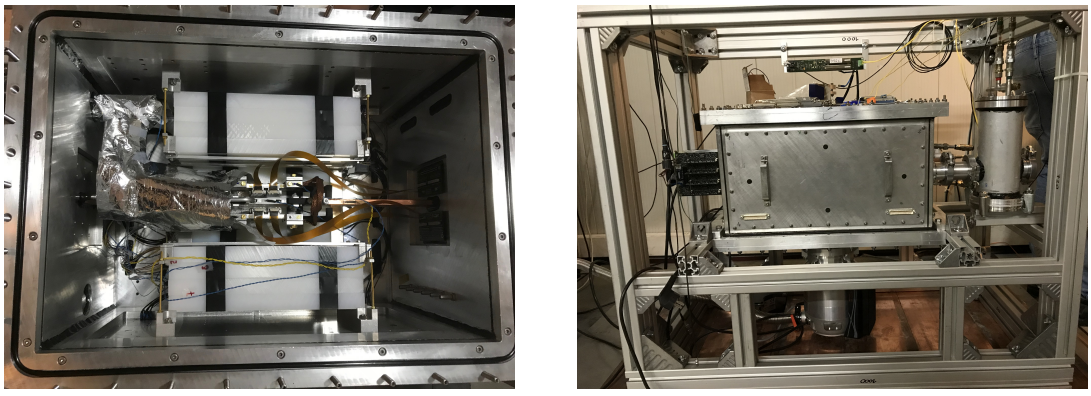

(a) Inside view of the vacuum chamber. (b) Outside view of the vacuum chamber.

Figure 4.1: Inside and outside view of the vacuum chamber.

The passive shielding blocks and the SDD readout boards, along with the connection to the cooling can be seen in Figure 4.2. Additionally, inside the vacuum chamber is where the four 2×4 SDDs and the seven PT-100 units are placed, along with the 100 A powered copper strip (Figure 4.3).

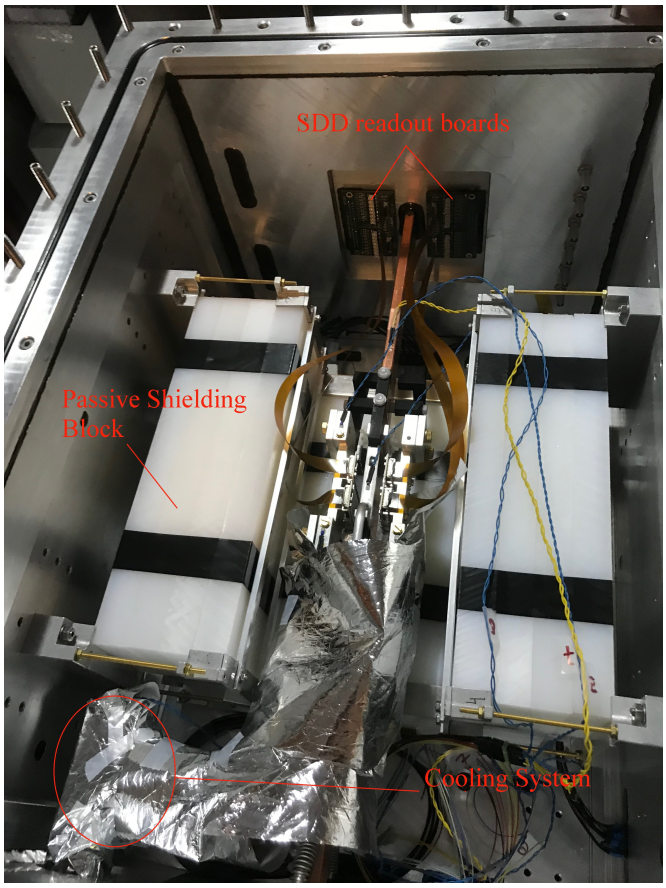

Figure 4.2: View of the passive shielding blocks, SDD readout boards and the connection to the cooling inside the vacuum chamber.

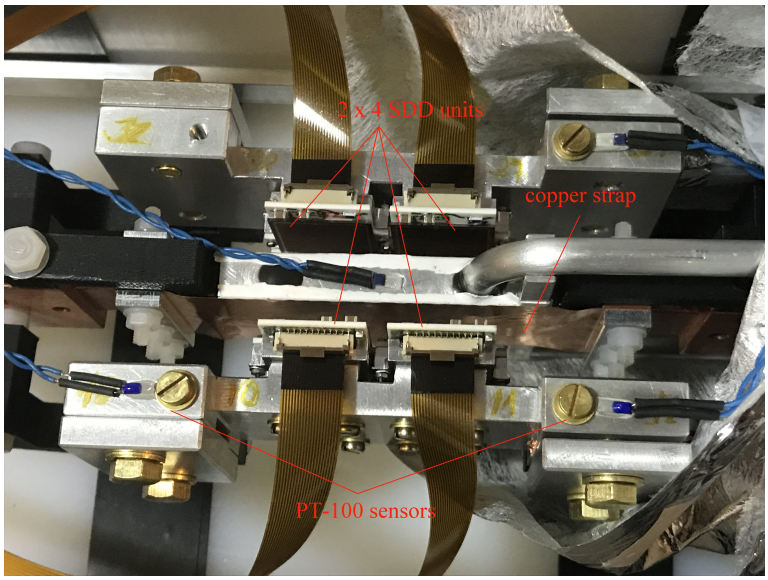

Figure 4.3: View of the 4 SDDs and 7 PT-100 units, along with the thin copper strap within the vacuum chamber.

The Polycold Compact Cooler (CryoTiger) is located outside of the vacuum chamber in addition to the SDD amplifier board. Furthermore, the vacuum chamber is connected to a Forepump and Turbo pump which are connected to the Data Acquisition (DAQ) system, thus completing the VIP2-Upgrade experimental setup (Figure 4.4).

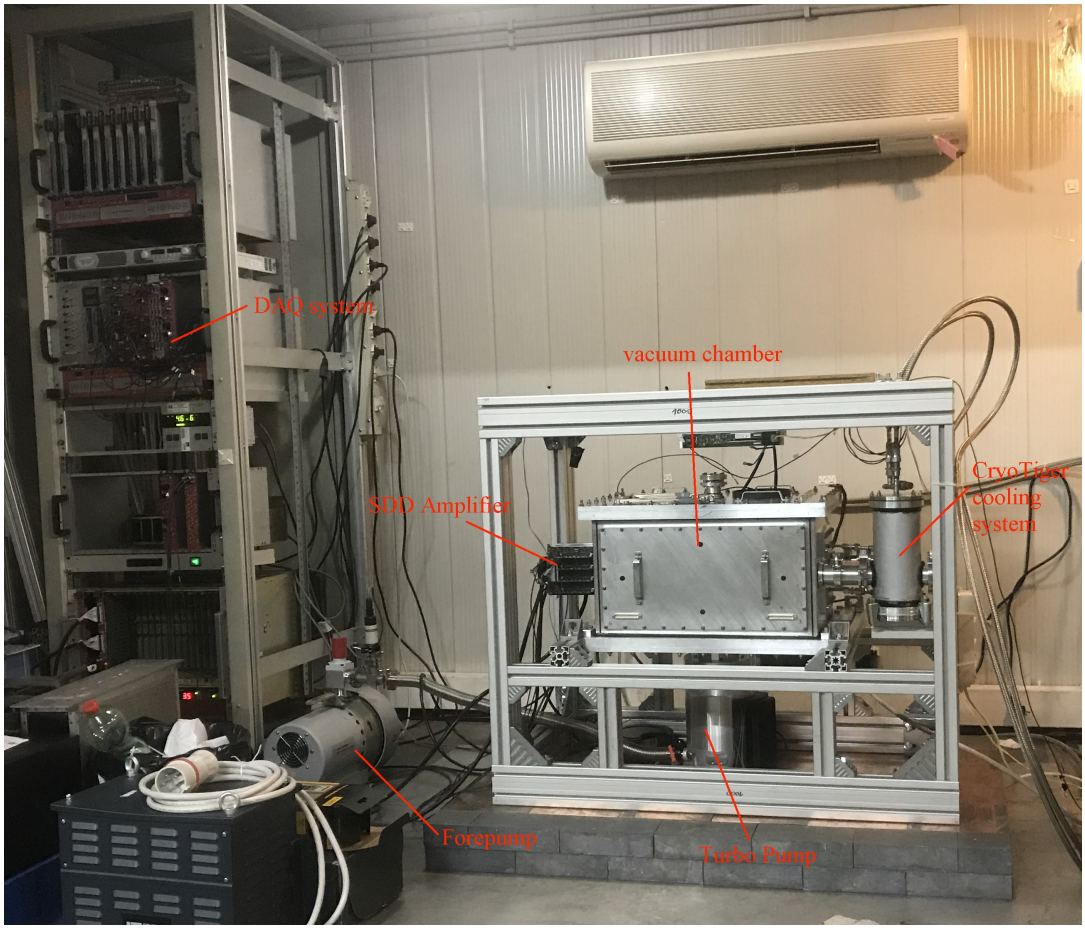

Figure 4.4: VIP2-Upgrade experimental setup.

4.1 Preliminary Results

Following the completion of the VIP2-Upgrade's experimental setup, the first few measurements were started and new data are being collected. To confirm that everything is functioning correctly, a preliminary measurement has been performed. In Figure 4.5 the energy spectrum of the measurement is shown.

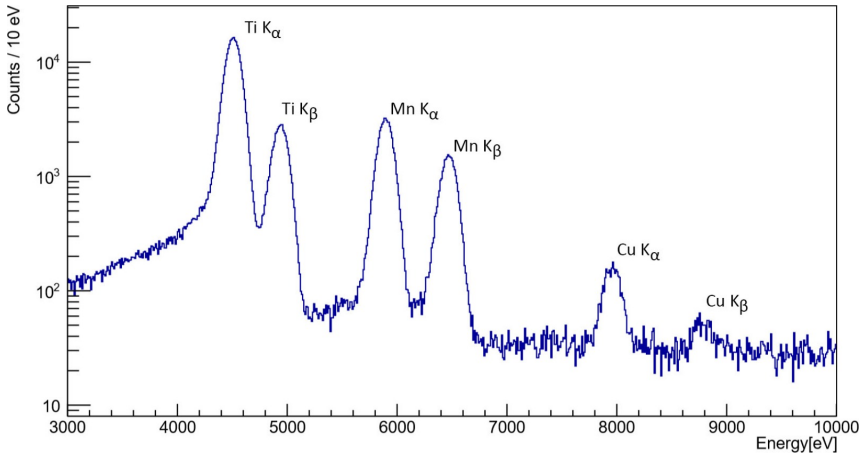

Figure 4.5: Energy spectrum of the preliminary test measurement for the VIP2-Upgrade experimental setup.

The reference peaks used for further data analysis (not part of this thesis) are the Mn K_α and K_β peaks along with the Ti and Cu K_α and K_β peaks. This preliminary result is consistent with the measurement results of the previous VIP2 experimental setup [see 5, chapter 6].

Chapter 5

Summary and Outlook

The goal of this thesis work was to implement some of the proposed changes for VIP-2 [12]. For those purposes all the individual components got tested and measurements were executed at the Stefan Meyer Institute (SMI). The test of the active shielding, used in the predecessor experiment VIP2, showed that almost a third of the Silicon Photomultipliers (SiPM) were not working properly. While the active shielding is being repaired or replaced, a passive shielding consisting of plastic blocks will be used. The proposed thermoelectric Peltier cooling could not deliver the needed performance to cool down the Silicon Drift Detectors (SDD) to a satisfactory level (around $-35°C$). Instead, the Polycold Compact Cooler (CryoTiger) will be used as it remained comfortably below $-35°C$ even with two separate heating resistors connected to the cold head via individual copper braids with heating powers up to 1.20 W, which is greater than the expected heat dissipation of the SDD array. New Silicon Drift Detectors (SDD) with a greater active area, compared to the SDDs used in the predecessor experiment VIP2, will be used. Additionally, a new slow control system to record temperature and pressure values and its operation, along with the Data Acquisition (DAQ) system and their functionality was verified. The vacuum chamber used in the predecessor experiment was tested at SMI and all leaks have been repaired. Finally, all these components were combined and the experimental setup was built. The setup was transported to the Laboratori Nazionali del Gran Sasso (LNGS) in March 2018 where it has been undergoing a lot of measurements to test its functionality. Ensuing these measurements a preliminary test has been performed and its result confirmed the functionality of the VIP2-Upgrade experimental setup.

The VIP2-Upgrade experimental setup is currently (November 2018) at LNGS, where further data will be taken. After around three more years of data taking, the anticipated new upper limit for the probability of the violation of the Pauli Exclusion Principle will be on the order of $10^{-30} - 10^{-31}$ or else, a violation of the Pauli Exclusion Principle will be discovered.

List of Figures

List of Tables

Bibliography

[1] M. Goldhaber and G. Scharff-Goldhaber. "Identification of Beta-Rays with Atomic Electrons". In: *Physical Review* 73(12) (June 1948), pp. 1472–1473.

[2] E. Ramberg and G. A. Snow. "Experimental limit on a small violation of the Pauli principle". In: *Physics Letters B* 238(2) (1990), pp. 438–441.

[3] C. Curceanu, S. Bartalucci, A. Bassi, et al. "Experimental tests of Quantum Mechanics: from Pauli Exclusion Principle Violation to spontaneous collapse models". In: *Journal of Physics: Conference Series* 361:012006 (2012).

[4] C. Curceanu, S. Bartalucci, A. Bassi, et al. "Experimental tests of quantum mechanics: Pauli Exclusion Principle Violation (the VIP experiment) and future perspectives". In: *Journal of Physics: Conference Series* 306(1):012036 (2011).

[5] Andreas Pichler. "Test of the Pauli exclusion principle for electrons in the Gran Sasso underground laboratory". PhD thesis. Vienna University of Technology, 2018. URL: http://katalog.ub.tuwien.ac.at/AC15028758.

[6] E. Gatti and P. Rehak. "Semiconductor drift chamber - An application of a novel charge transport scheme". In: *Nuclear Instruments and Methods in Physics Reseach* 225(3) (Sept. 1984).

[7] P. Lechner and H.Soltau. *Silicon Drift Detecotrs for SIDDHARTA - Mounting, Bonding and Testing*. Technical report.

[8] M. Cargnelli, M. Bragadi, M. Catitti, et al. "Silicon drift detectors for hadronic atom research - SIDDHARTA". In: *Proceedings, International Conference on Exotic Atoms and Related Topics (EXA 2005* (2005).

[9] W. Leo. *Techniques for Nuclear and Particle Physics Experiments*. Vol. 2 edition. 1993.

[10] AdvanSiD. AdvanSiD ASD-SiPM3S-P. Technical report. 2012.

[11] A. T. De Waele. "Pulse-tube refrigerators: principle, recent developments, and prospects". In: *Physica B: Condesed Matter* 280(1-4) (2000).

[12] J. Marton and A. Pichler. *Pauli Exclusion Principle test with electrons at LNGS - Continuation of FWF P25529-N20*. Tech. rep. 2017.

[13] C. Fiorini and R. Quaglia. *New developments of SDD-based X-ray detectors for the Siddharta-2 experiment*. Technical report. Politechnico di Milano, 2013.

[14] Doug Fike. *Polycold Compact Cooler (PCC) with PT Refrigerant Blends*. Operating Manual, Revision C. Brooks Automation Inc. 15 Elizabeth Drive, Chelmsford. MA 01824, 2014.

[15] Florian Buchner. Projektarbeit. 2018.

[16] A. Butt, G. Bellotti, M. Carminati, C. Fiorini, C. Piemonte, N. Zorzi, and F. Manca. "Characterization of monolithic SDD arrays and SFERA ASIC for the SIDDHARTA experiment". In: *Proc. IEEE NSS/MIC/RTSD* (Nov. 2016).

[17] C. Trippl. "Preparation of a High-precision X-ray Detector for Kaonic Atom Measurements at J-PARC and DAΦNE". MSc thesis. University of Vienna, 2018.

[18] A. Thompson et al. *X-ray data booklet*. Lawrence Berkley National Laboratory. 2009.

[19] National Instruments. *LabVIEW*. URL: http://www.ni.com/en-us/shop/labview.html.